Numerical methods for dynamic Magnetic Resonance Imaging

G. Landi, E. Loli Piccolomini

July 4, 2005

Contents

List of Tables

List of Figures

Chapter 1

Introduction to dynamic MRI

Magnetic Resonance Imaging (MRI) is a valuable non-invasive diagnostic tool used in medicine for acquiring cross sectional images of the human body. Dynamic MRI refers to the application of Magnetic Resonance (MR) to the study of a dynamic process: in order to capture the dynamic evolution, a time sequence of images of the same slice of the human body is acquired at high temporal rate. Dynamic MRI is often used in contrast–enhanced dynamic imaging or in functional brain studies. An emerging application field of dynamic MRI is interventional MRI, i.e. the use of MRI for planning, monitoring and guiding a medical intervention. In such dynamic applications of the MRI technique, temporal resolution is fundamental in order to completely capture the evolution of the imaged process. Unfortunately, there are technological and physiological limits on the MR technique that make difficult to simultaneously obtain high spatial and temporal resolution. The diagnostic efficiency of MRI is then seriously limited by the relatively long scan necessary for acquiring each image of the sequence. In the past years many methods have been introduced to fulfil the request for ever-faster dynamic MRI methods. Some of the proposed methods achieve high temporal resolution by sacrificing spatial resolution in the data acquisition process and they are therefore called *reduced encodings methods*. Such new methods include various and different methods; in this work we are considering a subset of reduced encodings methods constituted by zero padding-like methods [2], Keyhole-like methods [6, 15, 4, 8] and RIGR-like methods [8]. All these methods can be represented by a common numerical model [5] that theoretically unifies them and allows to conceptually understand their characteristics. Since high spatial resolution is desirable in order to have images of good quality, the imaging methods must supply the lack of acquired spatial information by incorporating *a priori* information about the imaged object into the reconstruction process. The various reduced encodings methods differ in how the missing high spatial frequencies are extrapolated, i.e. in how the *a priori* information is incorporated into the numerical model.
MRI is by its nature a Fourier encoded modality: the data are collected in the k-space, a frequency two-dimensional domain whose principal directions are called *frequency-encoded direction* (k_x) and *phase-encoded direction* (k_y). When the data of a dynamic MRI experiment are acquired with the spin-echo technique [11, 7], the k-space is sampled line by line and the data points on each line are equally spaced; in this way, the sample points coincide with a uniform rectangular grid. When this cartesian sampling

trajectory is followed, the images can be very quickly reconstructed by using a two-dimensional Discrete Inverse Fourier Transform (2DIFT) of the data. In the dynamic experiments, the data are usually uniformly sampled in time.
In the reduced encodings methods, the acquisition time is decreased by acquiring a time series of reduced *dynamic* data sets and one and/or two high-resolution *reference* data sets which are usually collected before and/or after the dynamic process. The reference data set acquired before the dynamic process is called *baseline* data set while the reference data set acquired after the dynamic process is called *active* data set. The reference data sets provide the *a priori* information on the imaged object. The dynamic data sets consist of a small and central part (a k-hole) of the k-space constituted by the low phase-encoded spatial frequencies: the dynamic data are undersampled in the k_y direction while they are fully encoded in the k_x direction. The rationale for truncating the dynamic data lies in the fact that the morphological details are mainly encoded by the high frequencies while the dynamic information is mainly contained in the low frequency part of the k-space. Thus, assuming that during the dynamic process no significant changes occur in the underlying morphology, the dynamic variation can be characterized by repeated sampling of the central k-hole. The information on the portion of the k-space uncollected during the dynamic process is derived from the reference data sets.
The reference images, i.e. the images corresponding to the reference data sets, are obtained by a two-dimensional Discrete Inverse Fourier Transform (2DIFT) of the reference data sets. When the data are undersampled along one direction of the k-space the images reconstructed by means of a 2DIFT suffer from the well-known truncation artifacts which include ringing and blurring. To overcome the impossibility of employing conventional Fourier techniques, the reduced encodings methods obtain dynamic images of good quality from the undersampled dynamic data sets by incorporating into the imaging process the *a priori* information deriving from the reference images.
In this work we present a unifying numerical model for representing the reduced encodings methods. The presented unifying model allows a comprehensive evaluation of the methods performance with respect to the dynamic MRI applications. Moreover, it explains how the various methods incorporates the *a priori* information into the imaging process in order to provide the missing high spatial frequencies. In the presented unifying approach, the unknown MR images are represented by means of a parametric model with basis functions; we explore the use of both exponential basis functions and B-spline basis functions. Exponential basis functions are traditionally used in literature for the reduced encodings methods. We have recently proposed the use of B–spline basis functions [12] in a parametric model for representing dynamic MR images and we extend here their use to the wider class of the reduced encodings methods. There is a variety of reasons for the use of B-splines as basis functions. The recursion formula by which they can be computed and the resulting computational efficiency make them an obvious and ideal choice for a parametric model. Moreover, B-splines have a smoothing effect on the noise that is always present in the acquired data in medical applications. Finally, B-splines are widely used for image fitting and representation (see [14] and the references therein). Furthermore, in order to reduce the presence of noise and truncation artifacts in the reconstructed dynamic images, we incorporate into the parametric model some "regularization strategies". Therefore, in this work, we describe a new approach to dynamic MRI in which a regularization term is included in the parametric model with B-spline basis functions.
The sequel is organized as follows. In chapter 2 the unifying model is introduced and then the different reduced encodings methods represented by the model are described. In chapter 3 the results of numer-

ous numerical experiments on both simulated and real MR data are presented in order to illustrate the performance of the methods described in chapter 2.

Chapter 2

Numerical methods

In this chapter we introduce a unifying framework for dynamic MRI in which the zero padding-like methods, the Keyhole-like methods and the RIGR-like methods are expressed by a common parametric equation. A unifying approach to dynamic MRI has been recently proposed by Tsao et al. [5] to treat the entire class of the reduced encodings methods; in this work we restrict our attention to the aforementioned methods and we propose the use of B-spline basis functions and regularization to improve the quality of the reconstructed dynamic MR images.
Before describing the model-based unifying approach, in the following section we formally describe the problem of dynamic MRI and we introduce the adopted notation.

2.1 The problem of dynamic MRI

In MRI two domains are considered: the data domain, the k-space, and the image domain. These domains are mutually related through the Fourier transform (figure 2.1). The k-space is a complex domain; its horizontal (k_x) and vertical (k_y) directions are frequency-encoded and phase-encoded directions, respectively. In spin-echo MR experiments, the k-space is built-up row-wise and the data are sampled on a 2D rectangular trajectory as shown in figure 2.2. The detected data, called *raw data*, are collected in a 2D k-space data matrix. Let Ω be the grid of points that fully cover the k-space:

$$\Omega = \{(n\Delta k_x, m\Delta k_y) \,|\, n = -N/2, \ldots, N/2-1,\, m = -M/2, \ldots, M/2-1\} \tag{2.1}$$

where Δk_x and Δk_y are machine-dependant sampling intervals. Let $D(n\Delta k_x, m\Delta k_y)$ be the k-space datum acquired at the grid point $(n\Delta k_x, m\Delta k_y)$; the detected data form a $N \times M$ matrix $D(\boldsymbol{k}_x, \boldsymbol{k}_y)$ whose (n,m)-th element is defined as:

$$\big(D(\boldsymbol{k}_x, \boldsymbol{k}_y)\big)_{n,m} = D(n\Delta k_x, m\Delta k_y), \quad (n\Delta k_x, m\Delta k_y) \in \Omega. \tag{2.2}$$

In a spin-echo experiment, the measured data matrix is first inverse Fourier transformed along the frequency-encoding direction, then the resulting spectra are inverse Fourier transformed along the phase-

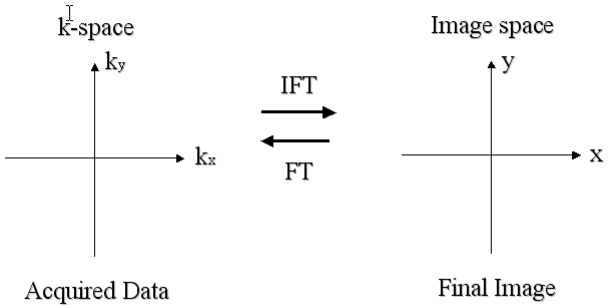

Figure 2.1: k-space and the MR image space

encoding direction yielding the desired image. Let $I(\boldsymbol{x}, \boldsymbol{y})$ be the $N \times M$ image reconstructed by a 2DIFT of the data matrix $D(\boldsymbol{k}_x, \boldsymbol{k}_y)$:

$$I(\boldsymbol{x}, \boldsymbol{y}) = \text{2DIFT}\left(D(\boldsymbol{k}_x, \boldsymbol{k}_y)\right) \tag{2.3}$$

defined as:

$$\big(I(\boldsymbol{x}, \boldsymbol{y})\big)_{j,i} = I(j\Delta x, i\Delta y), \quad j = 0, \ldots, N-1,\ i = 0, \ldots, M-1 \tag{2.4}$$

where

$$\Delta x = \frac{1}{N\Delta k_x}, \quad \Delta y = \frac{1}{M\Delta k_y} \tag{2.5}$$

and

$$I(j\Delta x, i\Delta y) = \frac{1}{NM} \sum_{n=-N/2}^{N/2-1} \sum_{m=-M/2}^{M/2-1} D(n\Delta k_x, m\Delta k_y) e^{2\sqrt{-1}\pi\left(\frac{n\,j}{N} + \frac{m\,i}{M}\right)} \tag{2.6}$$

for $j = 0, \ldots, N-1$, $i = 0, \ldots, M-1$.
The final MR image that is represented is the magnitude of $I(\boldsymbol{x}, \boldsymbol{y})$.

In a dynamic MRI experiment, the imaging time is decreased by only collecting the low spatial frequencies in the phase-encoded direction. Then, let Ω_{low} the grid points of the low-sampled k-space:

$$\Omega_{\text{low}} = \{(n\Delta k_x, m\Delta k_y)\,|\,n = -N_{\text{low}}/2, \ldots, N_{\text{low}}/2 - 1, m = -M/2, \ldots, M/2 - 1,\ N_{\text{low}} \ll N\}. \tag{2.7}$$

A sequence of low sampled dynamic $N_{\text{low}} \times M$ data matrices $D_t(\boldsymbol{k}_x, \boldsymbol{k}_y)$ defined as

$$\big(D_t(\boldsymbol{k}_x, \boldsymbol{k}_y)\big)_{n,m} = D_t(n\Delta k_x, m\Delta k_y), \quad (n\Delta k_x, m\Delta k_y) \in \Omega_{\text{low}}, \quad t = 1, \ldots, T, \tag{2.8}$$

is acquired at T successive time instants. Two fully encoded reference data sets are acquired to provide the information on the outer k-space region uncollected during the dynamic process. Let us denote

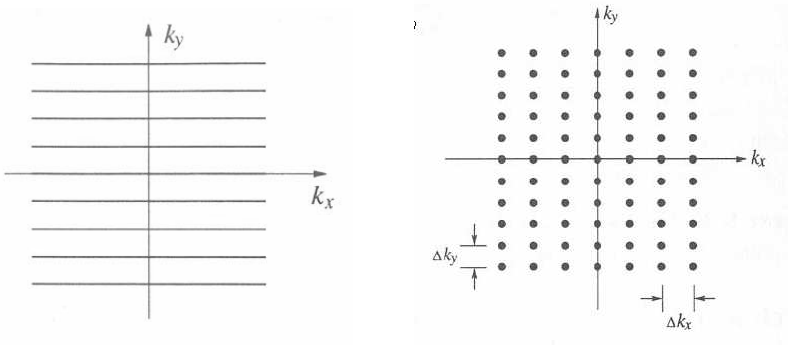

(a) Sampling trajectory (b) Raw data matrix

Figure 2.2: k-space sampling

$D_B(\boldsymbol{k}_x, \boldsymbol{k}_y)$ and $D_A(\boldsymbol{k}_x, \boldsymbol{k}_y)$ the $N \times M$ baseline and active reference data sets, respectively. The baseline and active reference images $I_B(\boldsymbol{x}, \boldsymbol{y})$ and $I_A(\boldsymbol{x}, \boldsymbol{y})$ are reconstructed by a 2DIFT:

$$I_B(\boldsymbol{x}, \boldsymbol{y}) = \text{2DIFT}\left(D_B(\boldsymbol{k}_x, \boldsymbol{k}_y)\right), \quad I_A(\boldsymbol{x}, \boldsymbol{y}) = \text{2DIFT}\left(D_A(\boldsymbol{k}_x, \boldsymbol{k}_y)\right). \tag{2.9}$$

The acquired dynamic data sets $D_t(\boldsymbol{k}_x, \boldsymbol{k}_y)$, $t = 1, \ldots, T$, are first inverse Fourier transformed along the fully encoded horizontal direction. Since the number of phase-encodings is reduced from N to N_{low}, performing a DIFT along the vertical direction gives images with evident truncation artifacts. A reconstruction method should solve this situation providing good quality high resolution images.
Let $\widehat{D}_t(\boldsymbol{k}_x, \boldsymbol{y})$ be the data matrix $D_t(\boldsymbol{k}_x, \boldsymbol{k}_y)$ transformed by DIFT along the rows:

$$\widehat{D}_t(n\Delta k_x, i\Delta y) = \frac{1}{M} \sum_{m=-M/2}^{M/2-1} D_t(n\Delta k_x, m\Delta k_y) e^{2\sqrt{-1}\pi\left(\frac{m\,i}{M}\right)} \tag{2.10}$$

with $n = -N_{\text{low}}/2, \ldots, N_{\text{low}}/2 - 1$, $i = 0, \ldots, M-1$.
A crucial point is that the dynamic image $I_t(\boldsymbol{x}, \boldsymbol{y})$ can be reconstructed column-wise from $\widehat{D}_t(\boldsymbol{k}_x, \boldsymbol{y})$ by reconstructing independently each column of $\widehat{D}_t(\boldsymbol{k}_x, \boldsymbol{y})$. In this way, the problem of reconstructing a $N \times M$ dynamic image is reduced to the problem of reconstructing M signals of size N.
Therefore, in the sequel, we will present the model-based approach to dynamic MRI only in the one dimensional case. The extension to the two dimensional case is immediate and is described in section 2.7. For easier notation, in the following sections, we omit the temporal index t. Specifically, we indicate with $D(\boldsymbol{k})$ a generic low sampled dynamic data vector of the sequence with elements:

$$\left(D(\boldsymbol{k})\right)_n = D(k_n), \quad k_n := n\Delta k, \quad n = \frac{-N_{\text{low}}}{2}, \ldots, \frac{N_{\text{low}}}{2} - 1. \tag{2.11}$$

Moreover, we denote with $I(\boldsymbol{x})$ a generic high resolution dynamic signal defined as

$$\left(I(\boldsymbol{x})\right)_j = I(x_j), \quad x_j := j\Delta x, \quad j = 0, \ldots, N-1, \tag{2.12}$$

where

$$\Delta x = \frac{1}{N\Delta k}. \tag{2.13}$$

Furthermore, $I(\widetilde{\boldsymbol{x}})$ denotes the low resolution dynamic signal obtained by a DIFT of the dynamic data set $D(\boldsymbol{k})$:

$$\big(I(\widetilde{\boldsymbol{x}})\big)_j = I(\widetilde{x}_j), \quad j = 0, \ldots, N_{\text{low}} - 1 \tag{2.14}$$

where

$$\widetilde{x}_j := j\Delta\widetilde{x}, \qquad \Delta\widetilde{x} = \frac{1}{N_{\text{low}}\Delta k} \tag{2.15}$$

and

$$I(\widetilde{x}_j) = \frac{1}{N_{\text{low}}} \sum_{n=-N_{\text{low}}/2}^{N_{\text{low}}/2-1} D(n\Delta k) e^{2\sqrt{-1}\pi\left(\frac{nj}{N}\right)} \tag{2.16}$$

with $j = 0, \ldots, N_{\text{low}} - 1$.
Finally, $D_B(\boldsymbol{k})$ ($D_A(\boldsymbol{k})$) indicates the baseline (active) reference data vector and $I_B(\boldsymbol{x})$ ($I_A(\boldsymbol{x})$) indicates the corresponding high resolution baseline (active) reference signal:

$$\big(D_A(\boldsymbol{k})\big)_n = D_A(k_n), \qquad \big(D_B(\boldsymbol{k})\big)_n = D_B(k_n), \quad n = -\frac{N}{2}, \ldots, \frac{N}{2} - 1, \tag{2.17}$$

$$\big(I_A(\boldsymbol{x})\big)_j = I_A(x_j), \qquad \big(I_B(\boldsymbol{x})\big)_j = I_B(x_j), \qquad j = 0, \ldots, N. \tag{2.18}$$

2.2 The unifying numerical model

In this section we present a model-based framework that unifies the wide class of the reduced encodings methods. In addition, we describe an algorithm for computing the model parameters.
The components $\big(I(\boldsymbol{x})\big)_j$ of the unknown dynamic signal are ideally the values of a continuous dynamic function $\mathcal{I}(x)$ at the points x_j:

$$\big(I(\boldsymbol{x})\big)_j = \mathcal{I}(x_j), \quad j = 0, \ldots, N - 1. \tag{2.19}$$

The unknown dynamic function $\mathcal{I}(x)$ can be factorized as:

$$\mathcal{I}(x) = \mathcal{I}_+(x) + \mathcal{I}_*(x) \cdot \mathcal{I}_d(x) \tag{2.20}$$

where $\mathcal{I}_+(x)$ and $\mathcal{I}_*(x)$ are additive and multiplicative constraints built into the model (2.20) for dynamic MRI. The function $\mathcal{I}_d(x)$ represents the dynamic features of $\mathcal{I}(x)$ not present in either $\mathcal{I}_+(x)$ or $\mathcal{I}_*(x)$. This function is represented by a parametric model as

$$\mathcal{I}_d(x) = \sum_{\ell=0}^{N_{\text{low}}-1} \alpha_\ell \phi_\ell(x). \tag{2.21}$$

The number of terms in the summation is determined by the number of available information on the desired dynamic signal, i.e. the number of acquired k-space dynamic data. The parametric model (2.21) for the dynamic function $\mathcal{I}_d(x)$ allows to select basis functions other than the complex exponential basis functions that are traditionally used in Fourier-based MRI. By substituting the representation (2.21) for $\mathcal{I}_d(x)$, equation (2.20) becomes:

$$\mathcal{I}(x) = \mathcal{I}_+(x) + \mathcal{I}_*(x) \cdot \sum_{\ell=0}^{N_{\text{low}}-1} \alpha_\ell \phi_\ell(x). \tag{2.22}$$

Equation (2.22) describes the wide class of the model-based reduced encodings methods in which, given the constraints functions $\mathcal{I}_+(x)$ and $\mathcal{I}_*(x)$ containing the *a priori* information and given the basis functions $\phi_0(x), \ldots, \phi_{N_{\text{low}}-1}(x)$, then every continuous dynamic signal $\mathcal{I}(x)$ is uniquely determined by the model parameters $\alpha_0, \ldots, \alpha_{N_{\text{low}}-1}$.
By discretizing the continuous equation (2.20) in the N points $x_0, \ldots, x_{N-1}$, we obtain the discrete model for the desired dynamic signal $I(\boldsymbol{x})$:

$$I(\boldsymbol{x}) = I_+(\boldsymbol{x}) + I_*(\boldsymbol{x}). * I_d(\boldsymbol{x}) \tag{2.23}$$

where $.*$ indicates the element-wise product and $I_+(\boldsymbol{x})$, $I_*(\boldsymbol{x})$ and $I_d(\boldsymbol{x})$ are discrete $N \times 1$ vectors containing, respectively, the values of $\mathcal{I}_+(x)$, $\mathcal{I}_*(x)$, and $\mathcal{I}_d(x)$ at the points x_j:

$$\big(I_+(\boldsymbol{x})\big)_j = \mathcal{I}_+(x_j), \quad j = 0, \ldots, N-1, \tag{2.24}$$

$$\big(I_*(\boldsymbol{x})\big)_j = \mathcal{I}_*(x_j), \quad j = 0, \ldots, N-1, \tag{2.25}$$

$$\big(I_d(\boldsymbol{x})\big)_j = \mathcal{I}_d(x_j), \quad j = 0, \ldots, N-1. \tag{2.26}$$

Following the continuous parametric model (2.21), the signal $I_d(\boldsymbol{x})$ is represented as:

$$I_d(\boldsymbol{x}) = \sum_{\ell=0}^{N_{\text{low}}-1} \alpha_\ell \phi_\ell(\boldsymbol{x}) \tag{2.27}$$

where

$$\phi_\ell(\boldsymbol{x}) = \big(\phi_\ell(x_0), \ldots, \phi_\ell(x_{N-1})\big)^t, \quad \ell = 0, \ldots, N_{\text{low}} - 1. \tag{2.28}$$

Therefore, equation (2.23) becomes:

$$I(\boldsymbol{x}) = I_+(\boldsymbol{x}) + I_*(\boldsymbol{x}). * \sum_{\ell=0}^{N_{\text{low}}-1} \alpha_\ell \phi_\ell(\boldsymbol{x}). \tag{2.29}$$

Equation (2.27) can be represented in matrix form as:

$$I_d(\boldsymbol{x}) = \Phi \boldsymbol{\alpha} \tag{2.30}$$

where Φ is the $N \times N_{\text{low}}$ matrix of the basis functions whose columns are the vectors $\phi_\ell(\boldsymbol{x})$:

$$\Phi = \begin{pmatrix} \phi_0(x_0) & \phi_1(x_0) & \dots & \phi_{N_{\text{low}}-1}(x_0) \\ \phi_0(x_1) & \phi_1(x_1) & \dots & \phi_{N_{\text{low}}-1}(x_1) \\ \vdots & \vdots & \ddots & \vdots \\ \phi_0(x_{N-1}) & \phi_1(x_{N-1}) & \dots & \phi_{N-1}(x_{N-1}) \end{pmatrix} \tag{2.31}$$

and the vector $\boldsymbol{\alpha}$ contains the coefficients values:

$$\boldsymbol{\alpha} = (\alpha_0, \dots, \alpha_{N_{\text{low}}-1})^t. \tag{2.32}$$

In the discrete setting, the vectors $I_+(\boldsymbol{x})$ and $I_*(\boldsymbol{x})$ are called *additive* and *multiplicative factors*, respectively. They are additive and multiplicative constraints used in model (2.23) to provide the *a priori* information necessary to compensate for the lack of low spatial frequencies encodings and to enable the reconstruction of high resolution signals from undersampled data. Better results are obtained by choosing constraint factors that are as close to the true dynamic signal as possible. In practice, the constraint factors are chosen to be the reference signals or a linear combination of them. If $I_+(\boldsymbol{x}) = \mathbf{0}$ and $I_*(\boldsymbol{x}) = \mathbf{1}$ where $\mathbf{0}$ and $\mathbf{1}$ are the vectors with components equal to 0 and 1, respectively, then no *a priori* information is used in the reconstruction process. The vector $I_d(\boldsymbol{x})$ is called *dynamic factor* and it accounts for the dynamic changes in the signal occurring during the dynamic evolution. Basically, the dynamic factor $I_d(\boldsymbol{x})$ is a signal with reduced details since it contains the dynamic information that are incomplete. The parametric model (2.21) for the continuous signal $\mathcal{I}(x)$ is the fundamental tool for reconstructing a high resolution dynamic factor $I_d(\boldsymbol{x})$ and, consequently, a high resolution dynamic signal $I(\boldsymbol{x})$ from a low resolution dynamic data set $D(\boldsymbol{k})$. In fact, given the additive and multiplicative factors $I_+(\boldsymbol{x})$ and $I_*(\boldsymbol{x})$ and selected a set of basis functions $\phi_0(x), \dots, \phi_{N_{\text{low}}-1}(x)$, the dynamic signal $I(\boldsymbol{x})$ can be computed from relation (2.29) *if* the coefficients $\alpha_0, \dots, \alpha_{N_{\text{low}}-1}$ are determined. In this way, the problem of reconstructing the dynamic signal $I(\boldsymbol{x})$ is converted to a coefficients estimation problem.
The crucial issue of determining the model coefficients $\alpha_0, \dots, \alpha_{N_{\text{low}}-1}$ is faced by fitting the dynamic signal $I_d(\boldsymbol{x})$ to the measured dynamic data $D(\boldsymbol{k})$. In particular, the parameter estimation problem is solved in two steps: first the low resolution version $I_d(\widetilde{\boldsymbol{x}})$ of the dynamic factor is determined and then, an interpolation problem is solved in order to obtain the model coefficients α_ℓ.
Specifically, let us consider the low resolution version $I(\widetilde{\boldsymbol{x}})$ of $I(\boldsymbol{x})$; for the signal $I(\widetilde{\boldsymbol{x}})$ equation (2.20) becomes :

$$I(\widetilde{\boldsymbol{x}}) = I_+(\widetilde{\boldsymbol{x}}) + I_*(\widetilde{\boldsymbol{x}}) .* I_d(\widetilde{\boldsymbol{x}}) \tag{2.33}$$

where $I_+(\widetilde{\boldsymbol{x}})$ and $I_*(\widetilde{\boldsymbol{x}})$ are the low resolution versions of the additive and multiplicative factors obtained by DIFT of the low frequencies part of their spectrum and

$$I_d(\widetilde{\boldsymbol{x}}) = \sum_{\ell=0}^{N_{\text{low}}-1} \alpha_\ell \phi_\ell(\widetilde{\boldsymbol{x}}) \tag{2.34}$$

with

$$\phi_\ell(\widetilde{\boldsymbol{x}}) = \big(\phi_\ell(\widetilde{x}_0), \dots, \widetilde{\phi}_\ell(\widetilde{x}_{N_{\text{low}}-1})\big)^t. \tag{2.35}$$

The data space is related to the signal space by means of the Fourier transform, therefore by applying the DFT to both the terms of (2.33), we obtain the expression

$$D(\boldsymbol{k}) = D_+(\boldsymbol{k}) + D_*(\boldsymbol{k}) \otimes D_d(\boldsymbol{k}) \tag{2.36}$$

where $\otimes$ represents the convolution product, $D(\boldsymbol{k})$ is the dynamic undersampled data set and

$$D_+(\boldsymbol{k}) = \mathrm{DFT}\big(I_+(\widetilde{\boldsymbol{x}})\big), \tag{2.37}$$

$$D_*(\boldsymbol{k}) = \mathrm{DFT}\big(I_*(\widetilde{\boldsymbol{x}})\big), \tag{2.38}$$

$$D_d(\boldsymbol{k}) = \sum_{\ell=0}^{N_{\mathrm{low}}-1} \alpha_\ell \mathrm{DFT}\big(\phi_\ell(\widetilde{\boldsymbol{x}})\big). \tag{2.39}$$

The convolution product in (2.36) can be represented in matrix form as

$$D(\boldsymbol{k}) = D_+(\boldsymbol{k}) + \mathcal{H}(D_*)D_d(\boldsymbol{k}) \tag{2.40}$$

where $\mathcal{H}(D_*)$ is a $N_{\mathrm{low}} \times N_{\mathrm{low}}$ matrix with Block Toeplitz structure constructed from the Fourier transform of the multiplicative factor $I_*(\boldsymbol{x})$:

$$\mathcal{H}(D_*) = \begin{pmatrix} D_*(0) & D_*(-1) & \dots & D_*(-N_{\mathrm{low}}+1) \\ D_*(1) & D_*(0) & \dots & D_*(-N_{\mathrm{low}}+2) \\ \vdots & \vdots & \ddots & \vdots \\ D_*(N_{\mathrm{low}}-1) & D_*(N_{\mathrm{low}}-2) & \dots & D_*(0) \end{pmatrix}. \tag{2.41}$$

Therefore, given $D_+(\boldsymbol{k})$ and $D_*(\boldsymbol{k})$, the unknown vector $D_d(\boldsymbol{k})$ is obtained by solving the linear system

$$\mathcal{H}(D_*)D_d(\boldsymbol{k}) = D(\boldsymbol{k}) - D_+(\boldsymbol{k}). \tag{2.42}$$

Since $\mathcal{H}(D_*)$ is relatively small (typically of size 64×64) and has hermitian Toeplitz structure, the system (2.42) can be solved efficiently.
The low resolution $N_{\mathrm{low}} \times 1$ dynamic factor $I_d(\widetilde{\boldsymbol{x}})$ is obtained by a DIFT of the computed data vector $D_d(\boldsymbol{k})$:

$$I_d(\widetilde{\boldsymbol{x}}) = \mathrm{DIFT}\big(D_d(\boldsymbol{k})\big). \tag{2.43}$$

Once the dynamic factor $I_d(\widetilde{\boldsymbol{x}})$ has been determined, the next step consists in calculating the model coefficients α_ℓ. The coefficients estimation problem is solved as an interpolation problem: the coefficients $\alpha_0, \dots, \alpha_{N_{\mathrm{low}}-1}$ are determined such that the continuous function $\mathcal{I}_d(x)$ interpolates the sample points $I_d(\widetilde{x}_0), \dots, I_d(\widetilde{x}_{N_{\mathrm{low}}-1})$:

$$\mathcal{I}_d(\widetilde{x}_j) = I_d(\widetilde{x}_j) \tag{2.44}$$

where $\mathcal{I}_d(x)$ is represented by the parametric model (2.21). Relation (2.44) is represented in matrix form as

$$\widetilde{\Phi}\boldsymbol{\alpha} = I_d(\widetilde{\boldsymbol{x}}) \tag{2.45}$$

where the coefficient matrix $\widetilde{\Phi}$ is the $N_{\text{low}} \times N_{\text{low}}$ matrix of the basis functions ϕ_ℓ sampled at the points $\widetilde{x}_j$:

$$\widetilde{\Phi} = \begin{pmatrix} \phi_0(\widetilde{x}_0) & \phi_1(\widetilde{x}_0) & \dots & \phi_{N_{\text{low}}-1}(\widetilde{x}_0) \\ \phi_0(\widetilde{x}_1) & \phi_1(\widetilde{x}_1) & \dots & \phi_{N_{\text{low}}-1}(\widetilde{x}_1) \\ \vdots & \vdots & \ddots & \vdots \\ \phi_0(\widetilde{x}_{N_{\text{low}}-1}) & \phi_1(\widetilde{x}_{N_{\text{low}}-1}) & \dots & \phi_{N_{\text{low}}-1}(\widetilde{x}_{N_{\text{low}}-1}) \end{pmatrix}. \tag{2.46}$$

The solution of the linear system (2.45) gives the desired model coefficients $\alpha_0, \dots, \alpha_{N_{\text{low}}-1}$. Actually the computation of the coefficients α_ℓ requires the solution of two linear systems: the first one (eq. (2.42)) is required for determining $I_d(\widetilde{\boldsymbol{x}})$ and the second one (eq. (2.45)) for computing the model parameters α_ℓ. When the coefficients $\alpha_0, \dots, \alpha_{N_{\text{low}}-1}$ are determined, the dynamic factor $I_d(\boldsymbol{x})$ is computed by relation (2.27) requiring a matrix-vector product. Finally, the dynamic signal $I(\boldsymbol{x})$ is computed by equation (2.23). It is evident that a large variety of methods can be derived from the introduced model-based equation (2.23) simply by choosing different factors $I_+(\boldsymbol{x})$ and $I_*(\boldsymbol{x})$ and basis functions $\phi_\ell(x)$ and by using different methods for estimating the model parameters α_ℓ.

Remark 1. We observe that the low resolution dynamic factor $I_d(\widetilde{\boldsymbol{x}})$ can be directly derived from equation (2.33) without solving any linear system:

$$I_d(\widetilde{\boldsymbol{x}}) = \big(I(\widetilde{\boldsymbol{x}}) - I_+(\widetilde{\boldsymbol{x}})\big)./I_*(\widetilde{\boldsymbol{x}}) \tag{2.47}$$

where ./ is the element-wise division. This approach for determining $I_d(\widetilde{\boldsymbol{x}})$ also suggested in [10], is less expensive but indeed less effective. If $I_d(\widetilde{\boldsymbol{x}})$ is given by (2.47), regularization is necessary to avoid divisions by zero and equation (2.47) is replaced by the modified equation

$$I_d(\widetilde{\boldsymbol{x}}) = \big(I(\widetilde{\boldsymbol{x}}) - I_+(\widetilde{\boldsymbol{x}})\big)./\big(I_*(\widetilde{\boldsymbol{x}}) + \lambda\big) \tag{2.48}$$

where λ is a small positive regularization parameter. Our experience indicates that the quality of the reconstructions obtained via equation (2.48) is degraded by evident artifacts depending on λ. Therefore, in the presented unifying approach, we follow equation (2.36) for reconstructing the dynamic factor because, in this case, the obtained $I_d(\widetilde{\boldsymbol{x}})$ is of better quality. Since the linear system (2.42) is a small size system, its solution is not computationally expensive; we still suggest to use equation (2.48) when computational problems arise in the solution of (2.42).

Remark 2. In practice, it is not necessary to compute the low resolution factors $I_+(\widetilde{\boldsymbol{x}})$ and $I_*(\widetilde{\boldsymbol{x}})$ to obtain the $N_{\text{low}} \times 1$ vectors $D_+(\boldsymbol{k})$ and $D_*(\boldsymbol{k})$. Let us consider the $N \times 1$ factors $I_+(\boldsymbol{x})$ and $I_*(\boldsymbol{x})$; the components $D_+(n\Delta k)$ and $D_*(n\Delta k)$ of their spectra are defined by a DFT:

$$D_+(n\Delta k) = \sum_{j=0}^{N-1} I_+(j\Delta x) e^{-2\sqrt{-1}\pi \frac{j\,n}{N}}, \quad n = -\frac{N}{2}, \dots, \frac{N}{2} - 1, \tag{2.49}$$

$$D_*(n\Delta k) = \sum_{j=0}^{N-1} I_*(j\Delta x) e^{-2\sqrt{-1}\pi \frac{j\,n}{N}}, \quad n = -\frac{N}{2}, \dots, \frac{N}{2} - 1, \tag{2.50}$$

where $\Delta x \Delta k = 1/N$. Then, $D_+(\boldsymbol{k})$ and $D_*(\boldsymbol{k})$ are the $N_{\text{low}} \times 1$ data vectors defined as:

$$\big(D_+(\boldsymbol{k})\big)_n = D_+(n\Delta k), \quad n = -\frac{N_{\text{low}}}{2}, \ldots, \frac{N_{\text{low}}}{2} - 1, \tag{2.51}$$

$$\big(D_*(\boldsymbol{k})\big)_n = D_*(n\Delta k), \quad n = -\frac{N_{\text{low}}}{2}, \ldots, \frac{N_{\text{low}}}{2} - 1. \tag{2.52}$$

We summarize this discussion by specifying the algorithm of the presented unifying model-based method for dynamic MRI.

Algorithm 2.1. *Unifying model-based algorithm for dynamic MRI.*

Input: dynamic data $D(\boldsymbol{k})$
additive factor $I_+(\boldsymbol{x})$
multiplicative factor $I_*(\boldsymbol{x})$
basis functions $\phi_0(x), \ldots, \phi_{N_{\text{low}}-1}(x)$
Output: dynamic signal $I(\boldsymbol{x})$

Step 1: Compute the spectra $D_+(\boldsymbol{k})$ and $D_*(\boldsymbol{k})$ (as in (2.51) and (2.52)) and the matrix $\mathcal{H}(D_*)$.

Step 2: Compute $D_d(\boldsymbol{k})$ by solving the linear system

$$\mathcal{H}(D_*)D_d(\boldsymbol{k}) = D(\boldsymbol{k}) - D_+(\boldsymbol{k}).$$

Step 3: Compute the low resolution dynamic factor $I_d(\widetilde{\boldsymbol{x}})$:

$$I_d(\widetilde{\boldsymbol{x}}) = \text{DIFT}\big(D_d(\boldsymbol{k})\big).$$

Step 4: Compute the basis functions matrix $\widetilde{\Phi}$ and compute the model coefficients vector $\boldsymbol{\alpha}$ by solving the linear system:

$$\widetilde{\Phi}\boldsymbol{\alpha} = I_d(\widetilde{\boldsymbol{x}}).$$

Step 5: Compute the basis functions matrix Φ and compute the high resolution dynamic factor $I_d(\boldsymbol{x})$:

$$I_d(\boldsymbol{x}) = \Phi\boldsymbol{\alpha}.$$

Step 6: Compute the high resolution dynamic signal $I(\boldsymbol{x})$:

$$I(\boldsymbol{x}) = I_+(\boldsymbol{x}) + I_*(\boldsymbol{x}) .* I_d(\boldsymbol{x}).$$

2.3 Choice of the basis and estimation of the model coefficients

In the unifying model (2.29), the dynamic factor $I_d(\boldsymbol{x})$ is represented in terms of continuous basis functions $\phi_\ell(x)$. Indeed, the reconstruction of the dynamic signal basically requires the solution of an interpolation problem: a set of continuous basis functions must be selected and the model coefficients must be determined. We have already stated that the model parameters are obtained from the solution of a linear system of equations. In this section we consider in detail the use of two classes of bases for signal representation: the Fourier basis and the B-spline basis; furthermore, we derive the algorithms for determining the model coefficients in both cases.

2.3.1 Fourier basis

The Fourier basis, traditionally used in MRI, uses a set of N_{low} complex exponential functions defined as

$$\phi_\ell(x) = e^{2\pi\sqrt{-1}(k_\ell x)} \tag{2.53}$$

where the discrete frequency index ℓ ranges from $-N_{\text{low}}/2$ to $N_{\text{low}}/2 - 1$.
With this choice of basis functions, the parametric model (2.21) becomes

$$\mathcal{I}_d(x) = \sum_{\ell=-N_{\text{low}}/2}^{N_{\text{low}}/2-1} \alpha_\ell e^{2\pi\sqrt{-1}(k_\ell x)} \tag{2.54}$$

where an index translation has been introduced in order to adapt the notation to the Discrete Fourier analysis traditional notation. In the discrete setting, for the low resolution dynamic factor $I_d(\widetilde{\boldsymbol{x}})$, equation (2.54) becomes:

$$I_d(\widetilde{x}_j) = \sum_{\ell=-N_{\text{low}}/2}^{N_{\text{low}}/2-1} \alpha_\ell e^{2\pi\sqrt{-1}\frac{j\,\ell}{N_{\text{low}}}}, \quad j = 0, \ldots, N_{\text{low}} - 1. \tag{2.55}$$

That is, the vector $\boldsymbol{\alpha} = (\alpha_{-N_{\text{low}}/2}, \ldots, \alpha_{N_{\text{low}}/2-1})^t$ is exactly:

$$\boldsymbol{\alpha} = \text{DFT}\big(I_d(\widetilde{\boldsymbol{x}})\big). \tag{2.56}$$

Therefore, from the relations (2.43) and (2.56), it immediately follows

$$D_d(\boldsymbol{k}) = \boldsymbol{\alpha}, \tag{2.57}$$

i.e. the model parameters $\alpha_{-N_{\text{low}}/2}, \ldots, \alpha_{N_{\text{low}}/2-1}$ represent the low frequencies of the dynamic factor $I_d(\boldsymbol{x})$. Namely, it is not necessary to solve the linear system (2.45) to estimate the model coefficients. The high resolution dynamic factor is obtained by padding with zeros the lacking high frequencies and then by applying a DIFT to the zero-filled spectrum. That is,

$$I_d(\boldsymbol{x}) = \text{DIFT}\Big(ZP\big(D_d(\boldsymbol{k})\big)\Big) \tag{2.58}$$

where $ZP\big(D_d(\boldsymbol{k})\big)$ indicates the zero-padded $N \times 1$ data vector:

$$ZP\big(D_d(\boldsymbol{k})\big) := (\ \underbrace{0,\ldots,0}_{\frac{N-N_{\text{low}}}{2}},\ \underbrace{D_d(\boldsymbol{k})}_{N_{\text{low}}},\ \underbrace{0,\ldots,0}_{\frac{N-N_{\text{low}}}{2}}\ ). \tag{2.59}$$

The Fourier basis is computationally advantageous because, if it is used in (2.21), the linear system (2.45) has not to be solved and $I_d(\boldsymbol{x})$ is merely reconstructed by a DIFT. However, the DIFT of a zero-padded vector yields a signal with substantial truncation artifacts degrading the quality of the reconstructed dynamic factor $I_d(\boldsymbol{x})$ and, consequently, of the dynamic signal $I(\boldsymbol{x})$.
The general algorithm 2.1 with Fourier basis can be stated as follows.

Algorithm 2.2. *Unifying model-based algorithm for dynamic MRI with Fourier basis.*

Input: dynamic data $D(\boldsymbol{k})$
additive factor $I_+(\boldsymbol{x})$
multiplicative factor $I_*(\boldsymbol{x})$
Output: dynamic signal $I(\boldsymbol{x})$

Step 1: Compute the spectra $D_+(\boldsymbol{k})$ and $D_*(\boldsymbol{k})$ and the matrix $\mathcal{H}(D_*)$.

Step 2: Compute $D_d(\boldsymbol{k})$ by solving the linear system

$$\mathcal{H}(D_*)D_d(\boldsymbol{k}) = D(\boldsymbol{k}) - D_+(\boldsymbol{k}).$$

Step 3: Compute the high resolution dynamic factor $I_d(\boldsymbol{x})$:

$$I_d(\boldsymbol{x}) = \text{DIFT}\Big(ZP\big(D_d(\boldsymbol{k})\big)\Big).$$

Step 4: Compute the high resolution dynamic signal $I(\boldsymbol{x})$:

$$I(\boldsymbol{x}) = I_+(\boldsymbol{x}) + I_*(\boldsymbol{x}).* I_d(\boldsymbol{x}).$$

2.3.2 B-spline basis

B-spline functions are polynomial functions forming a basis for the spline space; they give piecewise interpolation polynomials that are continuous everywhere and do not tend to oscillate in the case of high polynomial degree. Because of their compact support and other attractive numerical properties (fast evaluation of individual B-spline functions by a recursion relation, band-structured matrix of values,..), B-splines are a good choice for the interpolation problem. B-spline interpolation is accurate and has a relatively low computational cost, therefore the use of a B-spline basis is proposed as a valid alternative to

the usual Fourier basis in MR signal representation. In addition, a regularization procedure is introduced into the B-spline coefficients computation in order to reduce noise and artifacts in the reconstructed dynamic signal. The possibility of regularizing the model parameters $\alpha_{-N_{\rm low}/2},\ldots,\alpha_{N_{\rm low}/2-1}$ is a further advantage of the B-spline basis over the classic Fourier basis.
A basis of $N_{\rm low}$ normalized B-splines $\mathcal{B}_0^q(x),\ldots,\mathcal{B}_{N_{\rm low}-1}^q(x)$ of order q (and degree $q-1$) is defined as follows. Given the interpolation points $\widetilde{x}_0,\ldots,\widetilde{x}_{N_{\rm low}-1}$ in the interval $[0,(N_{\rm low}-1)/N_{\rm low}]$, let $\{t_j\}_{j=0}^{N_{\rm low}-1+q}$ be the extended knot partition of $[0,(N_{\rm low}-1)/N_{\rm low}]$ determined by the formula:

$$t_j=\begin{cases}\widetilde{x}_0, & j=0,\ldots,q-1;\\ \dfrac{1}{q-1}\displaystyle\sum_{i=j+1}^{j+q-1}\widetilde{x}_{i-q}, & j=q,\ldots,N_{\rm low}-1;\\ \widetilde{x}_{N_{\rm low}-1}, & j=N_{\rm low},\ldots,N_{\rm low}-1+q.\end{cases}\tag{2.60}$$

The j-th normalized B-spline $B_j^q(x)$, $j=0,\ldots,N_{\rm low}-1$, of order q has support $[t_j,t_{j+q}]$ and is defined by the recursion relation:

$$\mathcal{B}_j^s(x)=\begin{cases}\dfrac{x-t_j}{t_{j+s-1}-t_j}\mathcal{B}_j^{s-1}(x)+\dfrac{t_{j+s}-x}{t_{j+s}-t_{j+1}}\mathcal{B}_{j+1}^{s-1}, & \text{if } t_j\neq t_{j+s},\\ 0, & \text{otherwise,}\end{cases}\tag{2.61}$$

for $s=2,\ldots,q$, where

$$\mathcal{B}_j^1(x)=\begin{cases}1, & \text{if } t_j\le x<t_{j+1},\\ 0, & \text{otherwise.}\end{cases}\tag{2.62}$$

This important recursion formula shows that a B-spline of order $q>0$ is a linear blend of lower order B-splines. It also provides a stable and efficient means of evaluating the parametric model.
With the B-spline basis $\mathcal{B}_0^q(x),\ldots,\mathcal{B}_{N_{\rm low}-1}^q(x)$, the parametric model (2.21) becomes

$$\mathcal{I}_d(x)=\sum_{\ell=0}^{N_{\rm low}-1}\alpha_\ell\mathcal{B}_\ell^q(x).\tag{2.63}$$

The coefficients $\alpha_0,\ldots,\alpha_{N_{\rm low}-1}$ are determined by the linear system of equations (2.45) arising from the interpolation conditions. Since the knot partition (2.60) satisfies the Schoenberg-Whitney conditions [13], the coefficient matrix $\widetilde{\Phi}$ of the B-splines values is nonsingular and the interpolation problem (2.45) has a unique solution $\boldsymbol{\alpha}$. The coefficient matrix $\widetilde{\Phi}$ is always a band diagonal matrix of bandwidth q. Moreover, $\widetilde{\Phi}$ is usually smaller than a 64×64 matrix. Hence, (2.45) can be solved efficiently.
Three different approaches to the solution of (2.45) are considered. In the first one, the linear system (2.45) is solved by a direct method. Since the coefficient matrix $\widetilde{\Phi}$ is a small-size band diagonal matrix, the solution $\boldsymbol{\alpha}$ is efficiently computed by LU decomposition.

In the second and third approaches, a regularization method is used for computing the solution of the linear system (2.45). The rationale behind regularizing the model coefficients can be explained as follows. The dynamic function $\mathcal{I}_d(x)$ can be viewed as a parametric curve; in Computer Aided Geometric Design, the coefficients α_ℓ of the B-splines are called *control points* and the polygon obtained by connecting the adjacent control points is termed as *control polygon*. The B-splines serve the role of shape functions. The B-spline curve $\mathcal{I}_d(x)$ lies in the convex hull of its control polygon and its shape is defined and manipulated by the set of control points. The local support property of the B-splines implies that a change in a control point only affects a limited portion of the curve. These properties imply that the resulting curve $\mathcal{I}_d(x)$ is a smooth approximation of the control polygon and that the shape of the curve is determined by the position of its control points. Conversely, the control polygon can be thought as an approximation of the N_{low} values of the curve. Therefore, by computing the model coefficients by a regularization method, the entire curve $\mathcal{I}_d(x)$ is regularized by requiring that its control points α_ℓ take on a regular structure.
In the second approach, Tikhonov regularization method is used to solve (2.45): the coefficients vector $\boldsymbol{\alpha}$ is estimated by solving the unconstrained optimization problem

$$\min_{\boldsymbol{\alpha}} \quad \frac{1}{2}\|\widetilde{\Phi}\boldsymbol{\alpha} - I_d(\widetilde{\boldsymbol{x}})\|_2^2 + \frac{\lambda}{2}\|L\boldsymbol{\alpha}\|_2^2, \quad \lambda > 0 \tag{2.64}$$

where the positive regularization parameter λ is given. The objective function of (2.64) is made by two terms: the first one is a data fidelity term that measures the discrepancy between the values $I_d(\widetilde{x}_j)$ and $\mathcal{I}_d(x)$ at the grid points $\widetilde{x}_j$ and ensures that the model accurately represents the available samples. The second term is the regularization term that penalizes the presence of noise and artifacts in the reconstructed signal. Since MR signals are characterized by edges in connection of the tissue boundaries, the matrix L is the first order differential operator because it better preserves such discontinuities in the reconstructed signal. The regularization parameter λ controls the tradeoff between the fit of the data and the amount of regularization. The objective function is convex and attains its minimum at the solution of the Euler-Lagrange equations:

$$\big(\widetilde{\Phi}^t\widetilde{\Phi} + \lambda L^t L\big)\boldsymbol{\alpha} = \widetilde{\Phi}^t I_d(\widetilde{\boldsymbol{x}}). \tag{2.65}$$

In order to determine the model parameters $\alpha_0, \ldots, \alpha_{N_{\text{low}}-1}$, equation (2.65) has to be solved. The coefficient matrix $\widetilde{\Phi}^t\widetilde{\Phi} + \lambda L^t L$ is symmetric and positive definite; therefore, (2.65) is efficiently solved by Cholesky factorization. When the model coefficients are computed by solving (2.65), the resulting function $\mathcal{I}_d(x)$ is an approximate representation of the data because $\mathcal{I}_d(x)$ does not precisely interpolates the sample values $I_d(\widetilde{x}_j)$.
The third approach to the coefficients estimation consists in applying the truncated Conjugate Gradient (CG) method to the normal equations of (2.45):

$$\widetilde{\Phi}^t\widetilde{\Phi}\boldsymbol{\alpha} = \widetilde{\Phi}^t I_d(\widetilde{\boldsymbol{x}}) \tag{2.66}$$

as an iterative regularization method by stopping it after few iterations before noise and artifacts dominate in the solution. For easier notation we refer to this regularization strategy as CG regularization. Usually, the low resolution dynamic factor $I_d(\widetilde{\boldsymbol{x}})$ is contaminated by reconstruction and measurement errors and by artifacts. Let $I_d^{\text{exact}}(\widetilde{\boldsymbol{x}})$ be the noise-free dynamic factor and assume that an estimate σ of the error norm

$$\sigma \simeq \|I_d(\widetilde{\boldsymbol{x}}) - I_d^{\text{exact}}(\widetilde{\boldsymbol{x}})\|_2 \tag{2.67}$$

is known. Following the terminology conventionally used in the regularization framework, the error norm σ is referred to as *discrepancy*. The CG iterations are terminated as soon as the residual $r^{(p)}$ at the p-th iteration is less or equal to the discrepancy σ, i.e, when

$$r^{(p)} \leq \sigma. \tag{2.68}$$

The CGLS implementation [1] of the CG method when applied to the normal equations can be used for solving (2.66). This implementation is stable and does not require the matrix $\widetilde{\Phi}^t\widetilde{\Phi}$ to be explicitly formed. In practical dynamic MRI applications the discrepancy σ is unknown; numerical experiments have shown that good results are found after actually few iterations and that a high discrepancy value usually works well.
The computation of the coefficients vector $\boldsymbol{\alpha}$ with one of the aforesaid approaches leads to the computation of the high resolution dynamic factor

$$I_d(\boldsymbol{x}) = \Phi\boldsymbol{\alpha} \tag{2.69}$$

where Φ is the B-splines matrix at the grid points x_j. The high resolution dynamic signal $I(\boldsymbol{x})$ is then estimated:

$$I(\boldsymbol{x}) = I_+(\boldsymbol{x}) + I_*(\boldsymbol{x}).*I_d(\boldsymbol{x}). \tag{2.70}$$

The discussion of this section can be formalized in the following algorithm.

Algorithm 2.3. *Unifying model-based algorithm for dynamic MRI with B-spline basis.*

Input: dynamic data $D(\boldsymbol{k})$
additive factor $I_+(\boldsymbol{x})$
multiplicative factor $I_*(\boldsymbol{x})$
B-spline basis $\mathcal{B}_0^q(x), \ldots, \mathcal{B}_{N_{\text{low}}-1}^q(x)$
discrepancy σ
regularization parameter λ
Output: dynamic signal $I(\boldsymbol{x})$

Step 1: Compute the spectra $D_+(\boldsymbol{k})$ and $D_*(\boldsymbol{k})$ and the matrix $\mathcal{H}(D_*)$.

Step 2: Compute $D_d(\boldsymbol{k})$ by solving the linear system

$$\mathcal{H}(D_*)D_d(\boldsymbol{k}) = D(\boldsymbol{k}) - D_+(\boldsymbol{k}).$$

Step 3: Compute the low resolution dynamic factor $I_d(\widetilde{\boldsymbol{x}})$:

$$I_d(\widetilde{\boldsymbol{x}}) = \text{DIFT}\big(D_d(\boldsymbol{k})\big).$$

Step 4: Compute the B-splines matrix $\widetilde{\Phi}$ and compute the model coefficients vector $\boldsymbol{\alpha}$ with one of the following method:

1. **Direct method**: solve by LU decomposition the linear system:
$$\widetilde{\Phi}\boldsymbol{\alpha} = I_d(\widetilde{\boldsymbol{x}}).$$
2. **Tikhonov regularization**: solve by Cholesky decomposition the Tikhonov system:
$$\big(\widetilde{\Phi}^t\widetilde{\Phi} + \lambda L^t L\big)\boldsymbol{\alpha} = \widetilde{\Phi}^t I_d(\widetilde{\boldsymbol{x}}).$$
3. **CG regularization**: solve by truncated CG iterations the normal equations:
$$\widetilde{\Phi}^t\widetilde{\Phi}\boldsymbol{\alpha} = \widetilde{\Phi}^t I_d(\widetilde{\boldsymbol{x}}).$$

Step 5: Compute the B-splines matrix Φ and compute the high resolution dynamic factor $I_d(\boldsymbol{x})$:

$$I_d(\boldsymbol{x}) = \Phi\boldsymbol{\alpha}.$$

Step 6: Compute the high resolution dynamic signal $I(\boldsymbol{x})$:

$$I(\boldsymbol{x}) = I_+(\boldsymbol{x}) + I_*(\boldsymbol{x}) . * I_d(\boldsymbol{x}).$$

2.4 Methods not using *a priori* information: zero padding-like methods

In this section we describe the methods deriving from equation (2.23) when no *a priori* information is included into the model. In this case the additive and the multiplicative factors are chosen to be the vectors whose components are 0 and 1, respectively:

$$I_+(\boldsymbol{x}) = \mathbf{0} \quad \text{and} \quad I_*(\boldsymbol{x}) = \mathbf{1}. \tag{2.71}$$

With this choice of the constraint factors, the model equation (2.23) becomes:

$$I(\boldsymbol{x}) = I_d(\boldsymbol{x}), \tag{2.72}$$

namely, the dynamic signal $I(\boldsymbol{x})$ corresponds to the dynamic factor $I_d(\boldsymbol{x})$ and it is expressed by the parametric model

$$I(\boldsymbol{x}) = \sum_{\ell=0}^{N_{\text{low}}-1} \alpha_\ell \phi_\ell(\boldsymbol{x}). \tag{2.73}$$

Notice that the high resolution dynamic factor $I_d(\boldsymbol{x})$ is always reconstructed by methods for dynamic MRI not using *a priori* information. Hence, the analysis of the methods of this section is useful also to deeper understand the characteristics of all the methods described by the general equation (2.23).
Several methods not using *a priori* information are obtained with different choices of the basis functions $\phi_\ell(x)$ and with different approaches for determining the parameters α_ℓ. If the Fourier basis is used, equation (2.73) describes the *Zero Padding (ZP) method* [2]: the lacking dynamic high frequencies are assumed to be zero and the dynamic signal is reconstructed by applying a DIFT to the zero-filled data vector:

$$I(\boldsymbol{x}) = \text{DIFT}\Big(ZP\big(D(\boldsymbol{k})\big)\Big). \tag{2.74}$$

The algorithm of the zero padding method can be stated as follows.

Algorithm 2.4. *Zero padding method.*

Input: dynamic data $D(\boldsymbol{k})$
Output: dynamic signal $I(\boldsymbol{x})$

Step 1: Compute the high resolution dynamic signal $I(\boldsymbol{x})$:

$$I(\boldsymbol{x}) = \text{DIFT}\Big(ZP\big(D(\boldsymbol{k})\big)\Big).$$

When the B-spline basis is employed, different methods are obtained by using one of the three approaches described in section 2.3.2 for computing the basis coefficients α_ℓ. These methods are still called

zero padding methods to stress out that, as the traditional Fourier-based zero padding method, they are obtained from equation (2.23) without the use of the prior information provided by the constraint factors. The methods with B-spline basis are the following: *B-spline Zero Padding (BZP) method* with direct solution of the linear system (2.45), *B-spline Zero Padding method with Tikhonov regularization (BZP_Tik)*, and *B-spline Zero Padding method with CG regularization (BZP_CG)*.
The algorithm of the B-spline zero padding methods can be formally described as follows.

Algorithm 2.5. *B-spline zero padding methods.*

Input: dynamic data $D(\boldsymbol{k})$
B-spline basis $\mathcal{B}_0^q(x), \ldots, \mathcal{B}_{N_{\text{low}}-1}^q(x)$
discrepancy σ
regularization parameter λ
Output: dynamic signal $I(\boldsymbol{x})$

Step 1: Compute the low resolution dynamic signal

$$I(\widetilde{\boldsymbol{x}}) = \text{DIFT}\big(D(\boldsymbol{k})\big).$$

Step 2: Compute the B-splines matrix $\widetilde{\Phi}$ and compute the model coefficients vector $\boldsymbol{\alpha}$ with one of the following method:

1. **Direct method**: solve by LU decomposition the linear system:
$$\widetilde{\Phi}\boldsymbol{\alpha} = I(\widetilde{\boldsymbol{x}}).$$
2. **Tikhonov regularization**: solve by Cholesky decomposition the Tikhonov system:
$$\big(\widetilde{\Phi}^t\widetilde{\Phi} + \lambda L^t L\big)\boldsymbol{\alpha} = \widetilde{\Phi}^t I(\widetilde{\boldsymbol{x}}).$$
3. **CG regularization**: solve by truncated CG iterations the normal equations:
$$\widetilde{\Phi}^t\widetilde{\Phi}\boldsymbol{\alpha} = \widetilde{\Phi}^t I(\widetilde{\boldsymbol{x}}).$$

Step 3: Compute the B-splines matrix Φ and compute the high resolution dynamic signal I:

$$I(\boldsymbol{x}) = \Phi\boldsymbol{\alpha}.$$

The methods not using *a priori* information are summarized in the following table 2.1.

Method	**Basis**	$I_+(\boldsymbol{x})$	$I_*(\boldsymbol{x})$	**Approach to the model coefficients estimation problem**
ZP	Fourier	$\mathbf{0}$	$\mathbf{1}$	DIFT
BZP	B-spline	$\mathbf{0}$	$\mathbf{1}$	Direct method
BZP_Tik	B-spline	$\mathbf{0}$	$\mathbf{1}$	Tikhonov regularization
BZP_CG	B-spline	$\mathbf{0}$	$\mathbf{1}$	CG regularization

Table 2.1: Summary of zero padding-like methods.

2.5 Methods using *a priori* information: Keyhole-like methods

The methods discussed in this section are termed Keyhole-like methods from the Keyhole method [6, 15, 4, 8], the technique commonly implemented on commercial systems for dynamic MRI. The so called Keyhole-like methods are described by the common equation (2.23) when the *a priori* information is provided by the additive factor $I_+(\boldsymbol{x})$ and not by the multiplicative factor $I_*(\boldsymbol{x})$, i.e. when

$$I_+(\boldsymbol{x}) \neq \mathbf{0} \quad \text{and} \quad I_*(\boldsymbol{x}) = \mathbf{1}. \tag{2.75}$$

In this case, equation (2.23) becomes

$$I(\boldsymbol{x}) = I_+(\boldsymbol{x}) + I_d(\boldsymbol{x}) \tag{2.76}$$

where the dynamic factor $I_d(\boldsymbol{x})$ is expressed by the parametric model (2.27). Namely, the prior knowledge given by the baseline and/or the active reference signals is built into equation (2.23) only as an additive constraint. In this case, the dynamic factor represents the differences in the dynamic signal with respect to the additive factor:

$$I_d(\boldsymbol{x}) = I(\boldsymbol{x}) - I_+(\boldsymbol{x}). \tag{2.77}$$

The linear system (2.42) has not to be solved in order to determine the dynamic factor data $D_d(\boldsymbol{k})$; in fact, from (2.77) it immediately follows

$$D_d(\boldsymbol{k}) = D(\boldsymbol{k}) - D_+(\boldsymbol{k}). \tag{2.78}$$

Different Keyhole-like methods are obtained from the general equation (2.76) according to the selected basis functions, the method used for computing the coefficients α_ℓ and the chosen additive factor $I_+(\boldsymbol{x})$. As far as the choice of the basis is concerned, when the Fourier basis is employed (as in the traditional Keyhole method) the dynamic signal $I(\boldsymbol{x})$ is merely obtained by a DIFT of the completed $N \times 1$ dynamic data vector $D_d^{\text{compl}}(\boldsymbol{k})$ obtained by extrapolating from $D_+(\boldsymbol{k})$ the missing dynamic high frequencies:

$$\left(D_d^{\text{compl}}(\boldsymbol{k})\right)_n := \begin{cases} D_+(n\Delta k), & -\dfrac{N}{2} \leq n < \dfrac{N_{\text{low}}}{2}, \quad \dfrac{N_{\text{low}}}{2} - 1 < n \leq \dfrac{N}{2} - 1, \\ D(n\Delta k), & -\dfrac{N_{\text{low}}}{2} \leq n \leq \dfrac{N_{\text{low}}}{2} - 1. \end{cases} \tag{2.79}$$

In fact:

$$I(\boldsymbol{x}) = I_+(\boldsymbol{x}) + \mathrm{DIFT}\Big(ZP\big(D_d(\boldsymbol{k})\big)\Big) \tag{2.80}$$

$$= \mathrm{DIFT}\Big(D_+(\boldsymbol{k}) + ZP\big(D_d(\boldsymbol{k})\big)\Big) \tag{2.81}$$

$$= \mathrm{DIFT}\Big(D_+(\boldsymbol{k}) + ZP\big(D(\boldsymbol{k}) - D_+(\boldsymbol{k})\big)\Big) \tag{2.82}$$

and since

$$D_d^{\mathrm{compl}}(\boldsymbol{k}) = D_+(\boldsymbol{k}) + ZP\big(D(\boldsymbol{k}) - D_+(\boldsymbol{k})\big) \tag{2.83}$$

we have

$$I(\boldsymbol{x}) = \mathrm{DIFT}\Big(D_d^{\mathrm{compl}}(\boldsymbol{k}),\Big). \tag{2.84}$$

When the B-spline basis is chosen, the interpolation problem (2.45) has to be solved to compute the model coefficients α_ℓ. Possible choices of the additive factor are the following.

1. $I_+(\boldsymbol{x}) = I_B(\boldsymbol{x})$.
   The *a priori* information are provided by the high resolution baseline signal acquired before the dynamic process. If the Fourier basis is selected with this choice of $I_+(\boldsymbol{x})$, equation (2.76) reduces to the classic *KEYhole (KEY) method*: the missing dynamic high frequencies are extrapolated from the spectrum $D_B(\boldsymbol{k})$ of the baseline signal and $I(\boldsymbol{x})$ is reconstructed with a DIFT of the completed data vector. When the B-spline basis is employed, according to the method used for computing the model coefficients α_ℓ, we obtain the *B-spline KEYhole (BKEY) method* with direct solution of the linear system (2.45), the *B-spline KEYhole method with Tikhonov regularization (BKEY_Tik)*, and the *B-spline KEYhole method with CG regularization (BKEY_CG)*.

2. $I_+(\boldsymbol{x}) = I_W(t, \boldsymbol{x})$ where $I_W(t, \boldsymbol{x}) := \big(1 - \frac{1}{T+1}t\big)I_B(\boldsymbol{x}) + \big(\frac{1}{T+1}t\big)I_A(\boldsymbol{x})$, $t = 1, \ldots, T$.
   The additive factor $I_+(\boldsymbol{x})$ of the t-th signal $I(\boldsymbol{x}) := I_t(\boldsymbol{x})$, $t = 1, \ldots, T$, of the temporal sequence is a weighted combination of the baseline and active reference signals. In this case, $I_+(\boldsymbol{x})$ depends on the time instant t and, for the first signal of the sequence $I_+(\boldsymbol{x})$ is closer to $I_B(\boldsymbol{x})$, while, for the T-th signal, it is closer to $I_A(\boldsymbol{x})$. In this way, $I_+(\boldsymbol{x})$ is expected to better approximate the temporal evolution of the "true" additive factor of the t-th unknown exact dynamic signal. According to the chosen basis we obtain the *Weighted KEYhole method (WKEY)*, the *Weighted B-spline KEYhole method (WBKEY)* with direct solution of the linear system (2.45), the *Weighted B-spline KEYhole method with Tikhonov regularization (WBKEY_Tik)*, and the *Weighted B-spline KEYhole method with CG regularization (WBKEY_CG)* .

The algorithm of the Keyhole-like methods with Fourier basis can be stated as follows.

Algorithm 2.6. *Keyhole-like methods with Fourier basis.*

Input: dynamic data $D(\boldsymbol{k})$
additive factor $I_+(\boldsymbol{x}) = I_B(\boldsymbol{x})$ or $I_+(\boldsymbol{x}) = I_W(t, \boldsymbol{x})$
Output: dynamic signal $I(\boldsymbol{x})$

Step 1: Compute the spectrum $D_+(\boldsymbol{k})$.

Step 2: Compute the completed spectrum $D_d^{\text{compl}}(\boldsymbol{k})$ defined in (2.79).

Step 3: Compute the high resolution dynamic signal $I(\boldsymbol{x})$:

$$I(\boldsymbol{x}) = \text{DIFT}\Big(D_d^{\text{compl}}(\boldsymbol{k})\Big).$$

The algorithm of the Keyhole-like methods with B-spline basis is formally expressed as follows.

Algorithm 2.7. *Keyhole-like methods with B-spline basis.*

Input: dynamic data $D(\boldsymbol{k})$
additive factor $I_+(\boldsymbol{x}) = I_B(\boldsymbol{x})$ or $I_+(\boldsymbol{x}) = I_W(t, \boldsymbol{x})$
B-spline basis $\mathcal{B}_1^q(x), \ldots, \mathcal{B}_{N_{\text{low}}}^q(x)$
discrepancy σ
regularization parameter λ
Output: dynamic signal $I(\boldsymbol{x})$

Step 1: Compute the spectrum $D_+(\boldsymbol{k})$.

Step 2: Compute $D_d(\boldsymbol{k})$

$$D_d(\boldsymbol{k}) = D(\boldsymbol{k}) - D_+(\boldsymbol{k}).$$

Step 3: Compute the low resolution dynamic factor $I_d(\widetilde{\boldsymbol{x}})$:

$$I_d(\widetilde{\boldsymbol{x}}) = \text{DIFT}\big(D_d(\boldsymbol{k})\big).$$

Step 4: Compute the B-splines matrix $\widetilde{\Phi}$ and compute the model coefficients vector $\boldsymbol{\alpha}$ with one of the following method:

1. **Direct method**: solve by LU decomposition the linear system:

$$\widetilde{\Phi}\boldsymbol{\alpha} = I_d(\widetilde{\boldsymbol{x}}).$$

2. **Tikhonov regularization**: solve by Cholesky decomposition the Tikhonov system:

$$\big(\widetilde{\Phi}^t\widetilde{\Phi} + \lambda L^t L\big)\boldsymbol{\alpha} = \widetilde{\Phi}^t I_d(\widetilde{\boldsymbol{x}}).$$

3. **CG regularization**: solve by truncated CG iterations the normal equations:

$$\widetilde{\Phi}^t\widetilde{\Phi}\boldsymbol{\alpha} = \widetilde{\Phi}^t I_d(\widetilde{\boldsymbol{x}}).$$

Step 5: Compute the B-splines matrix Φ and compute the high resolution dynamic factor $I_d(\boldsymbol{x})$:

$$I_d(\boldsymbol{x}) = \Phi\boldsymbol{\alpha}.$$

Step 6: Compute the high resolution dynamic signal $I(\boldsymbol{x})$:

$$I(\boldsymbol{x}) = I_+(\boldsymbol{x}) + I_d(\boldsymbol{x}).$$

The Keyhole-like methods of this section are summarized in the following table 2.2.

Method	**Basis**	$I_+(\boldsymbol{x})$	$I_*(\boldsymbol{x})$	**Approach to the model coefficients estimation problem**
KEY	Fourier	$I_B(\boldsymbol{x})$	$\mathbf{1}$	DIFT
BKEY	B-spline	$I_B(\boldsymbol{x})$	$\mathbf{1}$	Direct method
BKEY_Tik	B-spline	$I_B(\boldsymbol{x})$	$\mathbf{1}$	Tikhonov regularization
BKEY_CG	B-spline	$I_B(\boldsymbol{x})$	$\mathbf{1}$	CG regularization
WKEY	Fourier	$I_W(t,\boldsymbol{x})$	$\mathbf{1}$	DIFT
WBKEY	B-spline	$I_W(t,\boldsymbol{x})$	$\mathbf{1}$	Direct method
WBKEY_Tik	B-spline	$I_W(t,\boldsymbol{x})$	$\mathbf{1}$	Tikhonov regularization
WBKEY_CG	B-spline	$I_W(t,\boldsymbol{x})$	$\mathbf{1}$	CG regularization

Table 2.2: Summary of the Keyhole-like methods.

2.6 Methods using *a priori* information: RIGR-like methods

The methods discussed in this section are classified as Reduced-encoded Imaging by Generalized-series Reconstruction (RIGR)-like methods because of their strong similarities with the RIGR method originally proposed by Liang and Lauterbur in [8] as an efficient technique for fast MRI. Successive developments of the RIGR method are the Two-references RIGR (TRIGR) [3] and the fast RIGR [10] methods. As the Keyhole technique, the original RIGR method is a Fourier imaging modality exploiting *a priori* information from the baseline signal. The difference between these methods lies in *how* the *a priori* information is used: as an additive constraint in the Keyhole method, and as a multiplicative constraint in the RIGR method. For this reason the RIGR method is more efficient and computationally more expensive than the Keyhole method. The use of the B-spline basis in the RIGR method has been introduced in [12] to improve the quality of the RIGR images.
The RIGR-like methods are obtained from the common equation (2.23) when the *a priori* information is encoded in the multiplicative factor and, eventually, in the additive factor; namely, when

$$I_*(\boldsymbol{x}) \neq \mathbf{1} \quad \text{and } \textit{eventually} \quad I_+(\boldsymbol{x}) \neq \mathbf{0}. \tag{2.85}$$

The model equation for this class of methods is therefore given by the general equation (2.23):

$$I(\boldsymbol{x}) = I_+(\boldsymbol{x}) + I_*(\boldsymbol{x}). * I_d(\boldsymbol{x}) \tag{2.86}$$

where

$$I_d(\boldsymbol{x}) = \sum_{\ell=0}^{N_{\text{low}}-1} \alpha_\ell \phi_\ell(\boldsymbol{x}). \tag{2.87}$$

Since $I_*(\boldsymbol{x}) \neq \mathbf{1}$, the linear system (2.42) has to be solved in order to compute $D_d(\boldsymbol{k})$ and consequently $I_d(\widetilde{\boldsymbol{x}})$. By choosing the Fourier basis or the B-spline basis and by selecting different factors $I_+(\boldsymbol{x})$ and $I_*(\boldsymbol{x})$, the various RIGR-like methods are obtained.
Possible choices of the additive factor are the following.

1. $I_+(\boldsymbol{x}) = \mathbf{0}$ and $I_*(\boldsymbol{x}) = |I_B(\boldsymbol{x})|$.
   If the Fourier basis is chosen with this choice of the factors, the classic RIGR method is obtained [9]. If the B-spline basis is used, by using different approaches for determining the basis coefficients, we obtain the *B-spline RIGR (BRIGR) method* with direct solution of the linear system (2.45) [12], the *B-spline RIGR method with Tikhonov regularization (BRIGR_Tik)*, and the *B-spline RIGR method with CG regularization (BRIGR_CG)* .

2. $I_+(\boldsymbol{x}) = I_B(\boldsymbol{x})$ and $I_*(\boldsymbol{x}) = |I_A(\boldsymbol{x}) - I_B(\boldsymbol{x})|$.
   The dynamic factor represents the changes of the dynamic signal with respect to the baseline one and the multiplicative factor encodes "difference" information into the model for $I(\boldsymbol{x})$. The *TRIGR* method [3] is obtained when the Fourier basis is employed; with the B-spline basis we obtain the *Two references B-spline RIGR (TBRIGR) method* with direct solution of the linear system (2.45) [12], the *Two references B-spline RIGR (TBRIGR_Tik) method with Tikhonov regularization*, and the *Two references B-spline RIGR method with CG regularization (TBRIGR_CG).*

3. $I_+(\boldsymbol{x}) = \mathbf{0}$ and $I_*(\boldsymbol{x}) = |I_W(t, \boldsymbol{x})|$, $t = 1, \ldots, T$.
   The multiplicative factor $I_*(\boldsymbol{x})$ of the t-th signal $I(\boldsymbol{x}) := I_t(\boldsymbol{x})$, $t = 1, \ldots, T$, of the temporal sequence is the absolute value of a weighted combination of the baseline and active reference signals. According to the selected basis we obtain the *Weighted RIGR (WRIGR) method*, the *Weighted B-spline (WBRIGR) RIGR method* with direct solution of the linear system (2.45), the *Weighted B-spline RIGR method with Tikhonov regularization (RIGR_Tik)*, and the *Weighted B-spline RIGR method with CG regularization (WRIGR_CG).*

The algorithm for the Fourier based RIGR-like methods is the same algorithm 2.2 of section 2.3.1 and it is repeated here for the reader's convenience.

Algorithm 2.8. *RIGR-like methods with Fourier basis.*

Input: dynamic data $D(\boldsymbol{k})$
additive factor $I_+(\boldsymbol{x})$ and multiplicative factor $I_*(\boldsymbol{x})$ such that:
$\Big(I_+(\boldsymbol{x}) = \mathbf{0}\ \&\ I_*(\boldsymbol{x}) = |I_B(\boldsymbol{x})|\Big)$ or $\Big(I_+(\boldsymbol{x}) = I_B(\boldsymbol{x})\ \&\ I_*(\boldsymbol{x}) = |I_A(\boldsymbol{x}) - I_B(\boldsymbol{x})|\Big)$
or $\Big(I_+(\boldsymbol{x}) = \mathbf{0}\ \&\ I_*(\boldsymbol{x}) = |I_W(t, \boldsymbol{x})|\Big)$

Output: dynamic signal $I(\boldsymbol{x})$

Step 1: Compute the spectra $D_+(\boldsymbol{k})$ and $D_*(\boldsymbol{k})$ and the matrix $H(D_*)$.

Step 2: Compute $D_d(\boldsymbol{k})$ by solving the linear system

$$H(D_*)D_d(\boldsymbol{k}) = D(\boldsymbol{k}) - D_+(\boldsymbol{k}).$$

Step 3: Compute the high resolution dynamic factor $I_d(\boldsymbol{x})$:

$$I_d(\boldsymbol{x}) = \mathrm{DIFT}\Big(ZP\big(D_d(\boldsymbol{k})\big)\Big).$$

Step 4: Compute the high resolution dynamic signal $I(\boldsymbol{x})$:

$$I(\boldsymbol{x}) = I_+(\boldsymbol{x}) + I_*(\boldsymbol{x}).*\, I_d(\boldsymbol{x}).$$

Analogously, algorithm 2.3 of section 2.3.2 is reviewed as follows for the B-splines based RIGR-like methods.

Algorithm 2.9. *RIGR-like methods with B-spline basis.*

Input: dynamic data $D(\boldsymbol{k})$
additive factor $I_+(\boldsymbol{x})$ and multiplicative factor $I_*(\boldsymbol{x})$ such that:
$\Big(I_+(\boldsymbol{x}) = \mathbf{0}\ \&\ I_*(\boldsymbol{x}) = |I_B(\boldsymbol{x})|\Big)$ or $\Big(I_+(\boldsymbol{x}) = I_B(\boldsymbol{x})\ \&\ I_*(\boldsymbol{x}) = |I_A(\boldsymbol{x}) - I_B(\boldsymbol{x})|\Big)$
or $\Big(I_+(\boldsymbol{x}) = \mathbf{0}\ \&\ I_*(\boldsymbol{x}) = |I_W(t, \boldsymbol{x})|\Big)$
B-spline basis $\mathcal{B}_1^q(x), \ldots, \mathcal{B}_{N_{\text{low}}}^q(x)$
discrepancy σ
regularization parameter λ
Output: dynamic signal $I(\boldsymbol{x})$

Step 1: Compute the spectra $D_+(\boldsymbol{k})$ and $D_*(\boldsymbol{k})$ and the matrix $H(D_*)$.

Step 2: Compute $D_d(\boldsymbol{k})$ by solving the linear system

$$H(D_*)D_d(\boldsymbol{k}) = D(\boldsymbol{k}) - D_+(\boldsymbol{k}).$$

Step 3: Compute the low resolution dynamic factor $I_d(\widetilde{\boldsymbol{x}})$:

$$I_d(\widetilde{\boldsymbol{x}}) = \mathrm{DIFT}\big(D_d(\boldsymbol{k})\big).$$

Step 4: Compute the B-splines matrix $\widetilde{\Phi}$ and compute the model coefficients vector $\boldsymbol{\alpha}$ with one of the following method:

1. **Direct method**: solve by LU decomposition the linear system:
$$\widetilde{\Phi}\boldsymbol{\alpha} = I_d(\widetilde{\boldsymbol{x}}).$$
2. **Tikhonov regularization**: solve by Cholesky decomposition the Tikhonov system:
$$\big(\widetilde{\Phi}^t\widetilde{\Phi} + \lambda L^t L\big)\boldsymbol{\alpha} = \widetilde{\Phi}^t I_d(\widetilde{\boldsymbol{x}}).$$
3. **CG regularization**: solve by truncated CG iterations the normal equations:
$$\widetilde{\Phi}^t\widetilde{\Phi}\boldsymbol{\alpha} = \widetilde{\Phi}^t I_d(\widetilde{\boldsymbol{x}}).$$

Step 5: Compute the B-splines matrix Φ and compute the high resolution dynamic factor $I_d(\boldsymbol{x})$:

$$I_d(\boldsymbol{x}) = \Phi\boldsymbol{\alpha}.$$

Step 6: Compute the high resolution dynamic signal $I(\boldsymbol{x})$:

$$I(\boldsymbol{x}) = I_+(\boldsymbol{x}) + I_*(\boldsymbol{x}).*I_d(\boldsymbol{x}).$$

The RIGR-like methods of this section are summarized in the following table 2.3.

Method	**Basis**	$I_+(\boldsymbol{x})$	$I_*(\boldsymbol{x})$	**Approach to the model coefficients estimation problem**
RIGR	Fourier	$\mathbf{0}$	$\lvert I_B(\boldsymbol{x})\rvert$	DIFT
BRIGR	B-spline	$\mathbf{0}$	$\lvert I_B(\boldsymbol{x})\rvert$	Direct method
BRIGR_Tik	B-spline	$\mathbf{0}$	$\lvert I_B(\boldsymbol{x})\rvert$	Tikhonov regularization
BRIGR_CG	B-spline	$\mathbf{0}$	$\lvert I_B(\boldsymbol{x})\rvert$	CG regularization
TRIGR	Fourier	$I_B(\boldsymbol{x})$	$\lvert I_A(\boldsymbol{x}) - I_B(\boldsymbol{x})\rvert$	DIFT
TBRIGR	B-spline	$I_B(\boldsymbol{x})$	$\lvert I_A(\boldsymbol{x}) - I_B(\boldsymbol{x})\rvert$	Direct method
TBRIGR_Tik	B-spline	$I_B(\boldsymbol{x})$	$\lvert I_A(\boldsymbol{x}) - I_B(\boldsymbol{x})\rvert$	Tikhonov regularization
TBRIGR_CG	B-spline	$I_B(\boldsymbol{x})$	$\lvert I_A(\boldsymbol{x}) - I_B(\boldsymbol{x})\rvert$	CG regularization
WRIGR	Fourier	$\mathbf{0}$	$\lvert I_W(t,\boldsymbol{x})\rvert$	DIFT
WBRIGR	B-spline	$\mathbf{0}$	$\lvert I_W(t,\boldsymbol{x})\rvert$	Direct method
WBRIGR_Tik	B-spline	$\mathbf{0}$	$\lvert I_W(t,\boldsymbol{x})\rvert$	Tikhonov regularization
WBRIGR_CG	B-spline	$\mathbf{0}$	$\lvert I_W(t,\boldsymbol{x})\rvert$	CG regularization

Table 2.3: Summary of RIGR-like methods.

The numerical methods for dynamic MRI described by the common equation (2.23) and introduced in sections 2.4, 2.5 and 2.6 are further summarized in table 2.4.

2.7 Extension to the two dimensional case

In real MRI applications, a dynamic *image* $I(\boldsymbol{x},\boldsymbol{y})$ has to be reconstructed from a dynamic data set $D(\boldsymbol{k_x},\boldsymbol{k_x})$ undersampled along the phase-encoding direction. Obviously, $I(\boldsymbol{x},\boldsymbol{y})$ ($D(\boldsymbol{k_x},\boldsymbol{k_x})$) belongs to a temporal sequence of images (data sets) but the temporal index is omitted here for easier presentation. One and/or two reference images are acquired before and/or after the dynamic process. As explained in section 2.1, the horizontal direction of $I(\boldsymbol{x},\boldsymbol{y})$ is first reconstructed by a DIFT and a matrix $\widehat{D}(\boldsymbol{k}_x,\boldsymbol{y})$ is obtained such that

$$\widehat{D}(n\Delta k_x, i\Delta y) = \frac{1}{M}\sum_{m=-M/2}^{M/2-1} D(n\Delta k_x, m\Delta k_y) e^{2\sqrt{-1}\pi\left(\frac{m\,i}{M}\right)}, \quad i = 0,\ldots,M-1. \tag{2.88}$$

Then each column $I(\boldsymbol{x},i\Delta y)$,$i = 0,\ldots,M-1$, of each image $I(\boldsymbol{x},\boldsymbol{y})$ of the succession is independently reconstructed by applying a method described by equation (2.23) to the corresponding column $\widehat{D}(\boldsymbol{k}_x,i\Delta y)$. The algorithm for the reconstruction of a generic dynamic image $I(\boldsymbol{x},\boldsymbol{y})$ of the temporal sequence is formally defined as follows.

Algorithm 2.10. *Unifying model-based algorithm for dynamic MR* ***image*** *reconstruction.*

Input: dynamic data set $D(\boldsymbol{k}_x, \boldsymbol{k}_y)$
additive factor $I_+(\boldsymbol{x}, \boldsymbol{y})$
multiplicative factor $I_*(\boldsymbol{x}, \boldsymbol{y})$
basis functions $\phi_0(x), \ldots, \phi_{N_{\text{low}}-1}(x)$
Output: dynamic image $I(\boldsymbol{x}, \boldsymbol{y})$

Step 1: Compute the spectra $\widehat{D}_+(\boldsymbol{k}_x, \boldsymbol{y})$ and $\widehat{D}_*(\boldsymbol{k}_x, \boldsymbol{y})$.

Step 1: Compute the basis functions matrices $\widetilde{\Phi}$ and Φ.

Step 2: Compute the matrix $\widehat{D}(\boldsymbol{k}_x, \boldsymbol{y}) = \text{DIFT}\big(D(\boldsymbol{k}_x, \boldsymbol{k}_y)\big)$.

Step 3: for $i = 0, \ldots, M-1$

3.1: Compute the matrix $\mathcal{H}(D_*)$ from the column vector $\widehat{D}_*(\boldsymbol{k}_x, i\Delta y)$.

3.2: Compute $\widehat{D}_d(\boldsymbol{k}_x, i\Delta y)$ by solving the linear system

$$\mathcal{H}(D_*)\widehat{D}_d(\boldsymbol{k}_x, i\Delta y) = \widehat{D}(\boldsymbol{k}_x, i\Delta y) - \widehat{D}_+(\boldsymbol{k}_x, i\Delta y).$$

3.3: Compute the column vector $I_d(\widetilde{\boldsymbol{x}}, i\Delta y)$ of the low resolution dynamic factor:

$$I_d(\widetilde{\boldsymbol{x}}, i\Delta y) = \text{DIFT}\big(\widehat{D}_d(\boldsymbol{k}_x, i\Delta y)\big).$$

3.4: Compute the model coefficients vector $\boldsymbol{\alpha}$ by solving the linear system:

$$\widetilde{\Phi}\boldsymbol{\alpha} = I_d(\widetilde{\boldsymbol{x}}, i\Delta y).$$

3.5: Compute the column vector $I_d(\boldsymbol{x}, i\Delta y)$ of the high resolution dynamic factor:

$$I_d(\boldsymbol{x}, i\Delta y) = \Phi\boldsymbol{\alpha}.$$

3.6: Compute column vector $I(\boldsymbol{x}, i\Delta y)$ of the high resolution dynamic image :

$$I(\boldsymbol{x}, i\Delta y) = I_+(\boldsymbol{x}, i\Delta y) + I_*(\boldsymbol{x}, i\Delta y). * I_d(\boldsymbol{x}, i\Delta y).$$

Class of the method	**Method**	**Basis**	$I_+(\boldsymbol{x})$	$I_*(\boldsymbol{x})$	**Approach to the model coefficients estimation problem**
Zero padding-like	ZP	Fourier	$\mathbf{0}$	$\mathbf{1}$	DIFT
	BZP	B-spline	$\mathbf{0}$	$\mathbf{1}$	Direct method
	BZP_Tik	B-spline	$\mathbf{0}$	$\mathbf{1}$	Tikhonov regularization
	BZP_CG	B-spline	$\mathbf{0}$	$\mathbf{1}$	CG regularization
Keyhole-like	KEY	Fourier	$I_B(\boldsymbol{x})$	$\mathbf{1}$	DIFT
	BKEY	B-spline	$I_B(\boldsymbol{x})$	$\mathbf{1}$	Direct method
	BKEY_Tik	B-spline	$I_B(\boldsymbol{x})$	$\mathbf{1}$	Tikhonov regularization
	BKEY_CG	B-spline	$I_B(\boldsymbol{x})$	$\mathbf{1}$	CG regularization
	WKEY	Fourier	$I_W(t,\boldsymbol{x})$	$\mathbf{1}$	DIFT
	WBKEY	B-spline	$I_W(t,\boldsymbol{x})$	$\mathbf{1}$	Direct method
	WBKEY_Tik	B-spline	$I_W(t,\boldsymbol{x})$	$\mathbf{1}$	Tikhonov regularization
	WBKEY_CG	B-spline	$I_W(t,\boldsymbol{x})$	$\mathbf{1}$	CG regularization
RIGR-like	RIGR	Fourier	$\mathbf{0}$	$\lvert I_B(\boldsymbol{x})\rvert$	DIFT
	BRIGR	B-spline	$\mathbf{0}$	$\lvert I_B(\boldsymbol{x})\rvert$	Direct method
	BRIGR_Tik	B-spline	$\mathbf{0}$	$\lvert I_B(\boldsymbol{x})\rvert$	Tikhonov regularization
	BRIGR_CG	B-spline	$\mathbf{0}$	$\lvert I_B(\boldsymbol{x})\rvert$	CG regularization
	TRIGR	Fourier	$I_B(\boldsymbol{x})$	$\lvert I_A(\boldsymbol{x}) - I_B(\boldsymbol{x})\rvert$	DIFT
	TBRIGR	B-spline	$I_B(\boldsymbol{x})$	$\lvert I_A(\boldsymbol{x}) - I_B(\boldsymbol{x})\rvert$	Direct method
	TBRIGR_Tik	B-spline	$I_B(\boldsymbol{x})$	$\lvert I_A(\boldsymbol{x}) - I_B(\boldsymbol{x})\rvert$	Tikhonov regularization
	TBRIGR_CG	B-spline	$I_B(\boldsymbol{x})$	$\lvert I_A(\boldsymbol{x}) - I_B(\boldsymbol{x})\rvert$	CG regularization
	WRIGR	Fourier	$\mathbf{0}$	$\lvert I_W(t,\boldsymbol{x})\rvert$	DIFT
	WBRIGR	B-spline	$\mathbf{0}$	$\lvert I_W(t,\boldsymbol{x})\rvert$	Direct method
	WBRIGR_Tik	B-spline	$\mathbf{0}$	$\lvert I_W(t,\boldsymbol{x})\rvert$	Tikhonov regularization
	WBRIGR_CG	B-spline	$\mathbf{0}$	$\lvert I_W(t,\boldsymbol{x})\rvert$	CG regularization

Table 2.4: Summary of methods for dynamic MRI.

Chapter 3

Tests and numerical experiments

In this chapter a wide experimentation of the methods described in chapter 2 is presented. The methods are tested on both simulated and real data. In the first part of the chapter (section 3.1) we present the results obtained with the methods that *do not use a priori information* (section 2.4), while in the second part of the chapter (section 3.2), we show the results obtained with the methods that *use a priori information* (sections 2.5 and 2.6). Usually, the second class of methods produce better images, because the additional information greatly contribute to the reconstruction process.

3.1 Methods not using *a-priori* information

In this section we present the results obtained in the reconstruction of simulated low-sampled MR data with the methods that do not use a priori information: the ZP method, the BZP method, the BZP_Tik method and the BZP_CG method. We have considered both one dimensional and two dimensional test problems. Aim of these tests is to show the effectiveness of the B-spline functions and of the regularization in smoothing both the artifacts and the noise. All the considered test problems confirm that B-spline functions are more suitable than the exponential functions for representing MR images and that the use of the regularization gives good results especially on noisy data. In the following, if not specified, the B-splines degree is 3.

One dimensional test problems

In this paragraph we present the results of two simulated one dimensional test problems. Given an exact high resolution dynamic signal $I^{\text{exact}}(\boldsymbol{x})$ of $N = 256$ components, the high resolution dynamic data set $D^{\text{exact}}(\boldsymbol{k})$ is obtained by a DFT of $I^{\text{exact}}(\boldsymbol{x})$; the undersampling of the data is simulated by considering only a subset $D(\boldsymbol{k})$ of the N_{low} lowest frequencies of the spectrum $D^{\text{exact}}(\boldsymbol{k})$.

The reconstruction methods described in section 2.4 are applied to the set $D(\boldsymbol{k})$ of N_{low} data frequencies in order to reconstruct the high resolution signal $I(\boldsymbol{x})$.

The noisy test problems are obtained by simulating the noise on the raw data $D(\boldsymbol{k})$, i.e. on the data in the Fourier space: white noise has been added to the N_{low} available frequencies before applying the

reconstruction algorithms.

The reconstructed signal $I(\boldsymbol{x})$ is compared to the true signal $I^{\text{exact}}(\boldsymbol{x})$. The results are represented by graphics; all the figures contain two graphics, the red dotted line representing the exact signal and the blue continuous line representing the reconstructed signal. As numerical error measures we use the Mean Square Error (MSE) and the Normalized Mean Average Error (NMAE) defined as:

$$\text{MSE} = \frac{1}{N}\sqrt{\sum_{i=1}^{N}(I^{\text{exact}}(x_i) - I(x_i))^2},$$
$$\text{NMAE} = \frac{\sum_{i=1}^{N}|I^{\text{exact}}(x_i) - I(x_i)|}{\sum_{i=1}^{N}|I^{\text{exact}}(x_i)|}.$$

For each test problem, the low resolution dynamic signal $I(\widetilde{\boldsymbol{x}})$, obtained by a DIFT of $D(\boldsymbol{k})$, is also shown. The considered test problems are the following.

Test problem TP1

The exact signal $I^{\text{exact}}(\boldsymbol{x})$ of the TP1 test problem is the box function plotted in figure 3.1(a); the low resolution $I(\widetilde{\boldsymbol{x}})$ signal obtained with $N_{\text{low}} = 64$ frequencies is represented in figure 3.1(b). Figures 3.2 and 3.3 show the reconstructions obtained with all the considered methods by B-splines of degree 3 and B-splines of degree 1, respectively; the ringing artifacts present in the ZP reconstructions are reduced when B-splines of degree 3 are used to represent the signal. The regularization introduces further smoothing effects on the oscillations, but in some cases it doesn't preserve the edges and peaks of the signal. In particular, Tikhonov regularization usually performs better than CG regularization. The regularization is more effective when low or medium noise is present on the data or when more frequencies are available. Figure 3.4 represents the behavior of the MSE and NMAE parameters with N_{low} varying from 8 to 128.

Table 3.1 reports the numerical values of the MSE and NMAE errors for the TP1 test problem. **Test problem TP2**.

The exact and low resolution signals $I^{\text{exact}}(\boldsymbol{x})$ and $I(\widetilde{\boldsymbol{x}})$ of the TP2 test problem are shown in figure 3.5(a) and 3.5(b) ($N_{\text{low}} = 64$), together with the low resolution noisy signals obtained when low noise and medium noise are added on the data (figure 3.5(c) and figure 3.5(d)). Figures 3.6 and 3.7 show the signals reconstructed with all the considered methods by using B-splines of degree 3 and degree 1 ($N_{\text{low}} = 64$), respectively. Figures 3.8 and 3.9 report the results obtained when $N_{\text{low}} = 128$ frequencies are considered. Finally, the MSE and NMAE parameters are plotted in figures 3.10 when N_{low} varies from 8 to 128; in figure 3.11, the MSE and NMAE parameters are computed for an increasing level of noise. These plots confirm the considerations of test problem TP1. The use of B-splines and regularization improves the quality of the reconstruction when N_{low} increases and when the data are affected by noise.

Two dimensional test problems

In this paragraph we present the results obtained when the previously discussed methods are applied to the images. In particular, we simulate MR images acquired by spin-echo technique, where each image row is acquired independently. Hence, the reconstruction methods are applied as described in section 2.7.

The noisy problems are obtained by simulating the presence of noise on the raw data. For each image row, white noise has been added on the N_{low} available frequencies before applying the reconstruction algorithm.

We consider two test images $I^{\text{exact}}(\boldsymbol{x}, \boldsymbol{y})$, the *phantom* and the *brain* images, each of size 256×256, showing different features. In order to simulate the k-space undersampling, a 2DFT has been applied to the test images to obtain the complete dynamic data sets $D^{\text{exact}}(\boldsymbol{k}_x, \boldsymbol{k}_y)$ of 256×256 samples; then the low sampled data sets $D(\boldsymbol{k}_x, \boldsymbol{k}_y)$ have been simulated by considering only a $N_{\text{low}} \times 256$ subset of the central lowest frequencies of $D^{\text{exact}}(\boldsymbol{k}_x, \boldsymbol{k}_y)$.

In the following, for each test problem, we show the reconstructed image $I(\boldsymbol{x}, \boldsymbol{y})$ and the *difference* image $I^{\text{diff}}(\boldsymbol{x}, \boldsymbol{y})$:

$$I^{\text{diff}}(\boldsymbol{x}, \boldsymbol{y}) = \text{abs}(I^{\text{exact}}(\boldsymbol{x}, \boldsymbol{y}) - I(\boldsymbol{x}, \boldsymbol{y}))$$

where $I^{\text{exact}}(\boldsymbol{x}, \boldsymbol{y})$ is the exact image. **Phantom test problem**

The exact image is shown in figure 3.12. We tested the methods by using $N_{\text{low}} = 128$, $N_{\text{low}} = 64$ and $N_{\text{low}} = 32$ frequencies.

The case $N_{\text{low}} = 64$ has been extensively treated. The ZP reconstruction (figure 3.13(a)) presents Gibbs artifacts, especially near the edges of the white circle and near the borders of the small black circles. The BZP reconstruction (figure 3.13(b)) smoothes the artifacts, and the use of regularization (figure 3.13(c), 3.13(d)) further reduces them. In particular, the reconstruction obtained with Tikhonov regularization is the best, while the reconstruction obtained with the CG method is blurred near the borders. The difference images represented in figure 3.14 confirm the previous considerations. When the data are noisy (figures 3.15- 3.18) the images reconstructed by the ZP method are affected by Gibbs artifacts and by noise, as it is evident in figures 3.16(a) and 3.18(a). Hence, the B-splines and the regularization act both on the Gibbs artifacts and on the noise.

When we consider $N_{\text{low}} = 128$ frequencies, the Gibbs artifacts are greatly reduced (figures 3.19, 3.20) in the absence of noise, while the noise is still present in the ZP reconstruction (figures 3.21, 3.22).

When $N_{\text{low}} = 32$, the reconstructions are low-quality images (figure 3.23, 3.24). Anyway, the difference between the methods behavior is enhanced: the use of B-splines smoothes the oscillations of the ZP reconstruction and Tikhonov regularization produces the best image.

Brain test problem

The exact image is obtained from real MR data and is shown in figure 3.25. In contrast with the *phantom* image, this image is characterized by many gray levels creating small objects with rather undefined edges. Figures 3.26 and 3.28 show the reconstructions obtained with $N_{\text{low}} = 64$ frequencies from no noisy and noisy data. Figures 3.27 and 3.29 show the difference images. The methods act as in the *phantom* test problem. We underline that the use of B-splines with Tikhonov regularization preserves the details even in this image and produces the best reconstructions again.

3.2 Methods using *a-priori* information

In this section we present the results obtained with the methods that use a priori information: the Keyhole-like methods (sec. 2.5) and the RIGR-like methods (sec. 2.6). Usually, the RIGR-like methods

produce better images , because the use of the *a priori* information as a multiplicative constraint gives an important contribution in the reconstruction process. We have considered one dimensional and two dimensional test problems with both simulated and real data.

One dimensional test problems

The one dimensional test problems are test problems on simulated data; we have considered two signals of 256 samples, representing the reference $I_B(\boldsymbol{x})$ and the exact dynamic signal $I^{\text{exact}}(\boldsymbol{x})$, respectively. The DFT of the signals gives the reference data $D_B(\boldsymbol{k})$ and the dynamic high resolution data $D^{\text{exact}}(\boldsymbol{k})$; the low sampling of the dynamic data set is simulated by considering, in the reconstruction process, only the N_{low}, ($N_{\text{low}} < 256$) dynamic lowest frequencies.
The considered simulated one dimensional test problems are the following.

Test problem TP3

In figure 3.30 the reference signal and the dynamic signal of the test problem TP3 are shown. The dynamic signal is reconstructed by only using N_{low} ($N_{\text{low}} = 16, 32, 64$) frequencies and the results are reported in figure 3.31 and 3.32. From the figure 3.31 it is evident that the use of B-splines of degree 3 and degree 1 reduces the oscillations of the Keyhole method. Furthermore, the use of regularization smoothes the peaks at the edges of the signal. Figure 3.32 shows the reconstructions obtained with the RIGR-like methods. The use of B-spline basis functions and regularization leads to the best reconstruction (figures 3.32(b), 3.32(e), 3.32(h), 3.32(k)) for the different values of N_{low}.

Test problem TP4

The reference and the dynamic signal of the TP4 test problem are plotted in figure 3.33. Figure 3.34 and 3.35 show the reconstructions. The considerations made for the test problem TP3 are still true in this case, and the *BRIGR_Tik* method shows the best performance.

Test problem TP5

Figure 3.36 shows the reference and exact dynamic signal of test problem TP5; in this case we have tested the methods on the noisy data of the signal plotted in 3.36(c). The noise has been added on dynamic frequencies, because in the real applications the acquired dynamic data generally suffer from the effects of the object moving during the data acquisition.
The smoothing effects of the regularization are more evident in this case than in the test problems TP3 and TP4 and the *BRIGR_Tik* method is still the best performing method (figures 3.38(b), 3.38(e), 3.38(h), 3.38(k)).

Two dimensional test problems

The methods have been tested on the following two test problems.

Circle test problem

The *circle* test problem is a test problem on simulated data. Two images of size 256×256 represent the reference image $I_B(\boldsymbol{x}, \boldsymbol{y})$ and the exact dynamic image $I^{\text{exact}}(\boldsymbol{x}, \boldsymbol{y})$, respectively. After Fourier transforming $I^{\text{exact}}(\boldsymbol{x}, \boldsymbol{y})$, a reduced scan spin-echo acquisition is simulated by considering the $N_{\text{low}} \times 256$ ($N_{\text{low}} = 64$) dynamic lowest frequencies. The reconstructed dynamic image $I(\boldsymbol{x}, \boldsymbol{y})$ is compared with the exact one and we can represent the difference image $I^{\text{diff}}(\boldsymbol{x}, \boldsymbol{y})$.
Figure 3.39 shows the reference $I_B(\boldsymbol{x}, \boldsymbol{y})$ and the exact dynamic image $I^{\text{exact}}(\boldsymbol{x}, \boldsymbol{y})$ of the *circle* test

problem. This problem is used in literature to represent, through the variations of gray levels in the dynamic image, the action of a contrast agent in the organ examined by the MR exam. The problem has been extensively examined and both the reconstructed dynamic images and the difference images are represented in all the performed tests. Figures 3.40 and 3.41 show the reconstructions obtained with the Keyhole-like methods ($N_{\text{low}} = 64$) and with the RIGR-like methods ($N_{\text{low}} = 64$), respectively, while the difference images are plotted in figures 3.42 and 3.43. The Gibbs artifacts in the Keyhole reconstruction (figure 3.40(a)) are reduced by the use of B-splines (figure 3.40(b)) and of regularization (figure 3.40(c)), even if an error is evident near the borders of the big circle (figures 3.42(a),3.42(b),3.42(c)). The BRIGR method with regularization (figures 3.41(c) and 3.43(c)) performs better and considerably reduces the errors near the border. When the methods are applied to noisy data (figures 3.44-3.47), the regularization is necessary to reduce not only the Gibbs artifacts but also the noise in the reconstructed images.

Mouse test problem: real MR data

The data for this test problem have been downloaded from the site:*http://mri.ifp.uiuc.edu/V/*. They are constituted of 6 data sets from a mouse breast with a big tumor: a baseline reference data set $I_B(\boldsymbol{x}, \boldsymbol{y})$ and an active reference data set $I_A(\boldsymbol{x}, \boldsymbol{y})$ of 256×256 samples (figure 3.48) and four low-sampled data sets of 64×256 samples, one for each dynamic section, acquired by a MR spin-echo technique after injecting a contrast agent. In figures 3.3-3.56 the reconstructions (and difference images) of the section 3 of the sequence are reported, when only the $I_B(\boldsymbol{x}, \boldsymbol{y})$ reference image is used. In this case, the reconstructions obtained with the Keyhole-like methods (KEY, BKEY, BKEY_Tik) are quite different from those obtained with the RIGR-like methods (RIGR, RIGR_Tik, BRIGR, BRIGR_Tik). The reason is that the reference image is used in a different way in the two classes of methods and some imperfections of the reference image, such as small black holes, are amplified in the images reconstructed by the RIGR-like methods (figures 3.50(a)-3.50(c) and 3.54(a)-3.54(c)). On the other side, the KEY images present artifacts as horizontal stripes along the low-sampled direction; the use of B-splines and especially the use of regularization greatly reduces the artifacts and the BKEY_Tik image is quite good ($N_{\text{low}} = 64$ or $N_{\text{low}} = 32$, figures 3.49(c) and 3.53(c)). Finally, the two references images $I_B(\boldsymbol{x}, \boldsymbol{y})$ and $I_A(\boldsymbol{x}, \boldsymbol{y})$, have been used and the reconstruction methods have been tested on three dynamic images of the sequence (sections $1, 3, 4$). Figures 3.3, 3.58 and 3.59 show the images obtained by the TBRIGR_Tik, WBKEY_Tik and WBRIGR_Tik, respectively. In all cases it is evident that the reconstructed images are better than those obtained with only one reference image; moreover, the quality of the WBKEY_Tik images is very good.

We can conclude that even in this test problem with real MR data, the use of B-splines and regularization gives very good results in terms of image quality. Moreover, the WBKEY_Tik method is computationally much more convenient than the RIGR-like methods as it is evident from the description reported in sections 2.5 and 2.6.

3.3 Considerations

We conclude this section with some global considerations on the performed numerical tests. In this report we propose the use of B-spline functions for the representation of MR signals and images and the use of regularization in the reconstruction of images from MR raw data.

In the first phase of the tests we have only considered the methods that *do not use a priori* information in the reconstruction of simulated low-sampled MR data. Aim of this phase was to show the effectiveness of B-spline functions and regularization in smoothing the artifacts and the noise in the MR signals and images. All the considered test problems confirmed that the B-spline functions are more suitable than the exponential functions for representing MR images and that the regularization gives good results especially on noisy data.
In the second phase of the tests we have considered methods that *use a priori* information encoded in the reference images acquired at the beginning and/or at the end of the dynamic sequence. The methods can be split into two classes: the Keyhole-like methods and the RIGR-like methods. Each class contains methods with Fourier and B-spline basis functions for the images representation and with regularization methods for the solution of the linear systems involved (see the methods description in chapter 2).
The methods are tested both on simulated and real MR data. The use of B-spline basis functions and of regularization enhances the Keyhole-like methods performance at a low computational cost. This seems the best solution for fast reconstruction of a high resolution MR sequence. The RIGR-like methods performs well when the reference images are of very high quality; anyway they are computationally more expensive than the Keyhole-like methods.

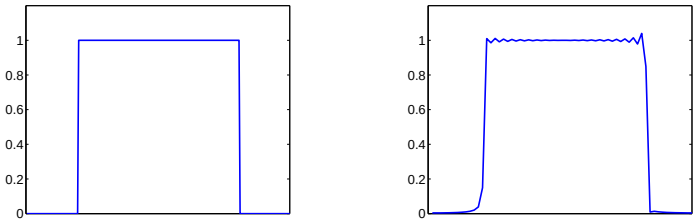

(a) Exact signal (b) Low resolution signal

Figure 3.1: Test problem TP1 ($N_{\text{low}} = 64$).

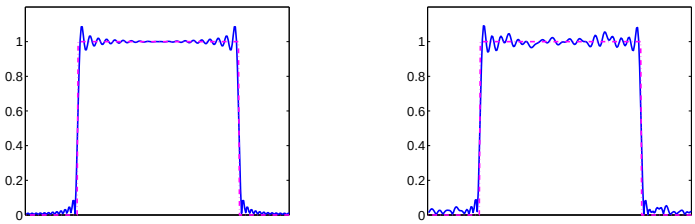

(a) ZP

(b) Noise ZP

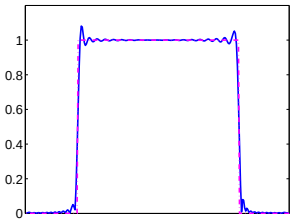

(c) BZP

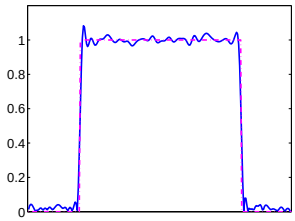

(d) Noise BZP

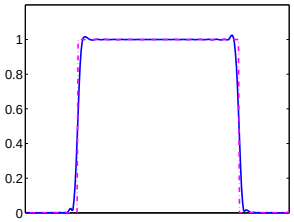

(e) BZP_Tik

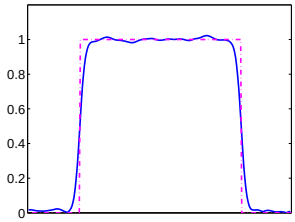

(f) Noise BZP_Tik

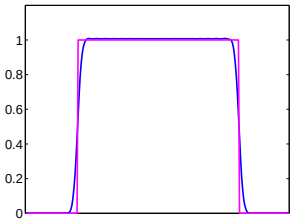

(g) BZP_CG

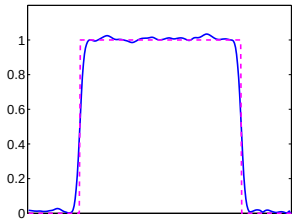

(h) Noise BZP_CG

Figure 3.2: Test problem TP1, B-splines of degree 3 ($N_{\text{low}} = 64$).

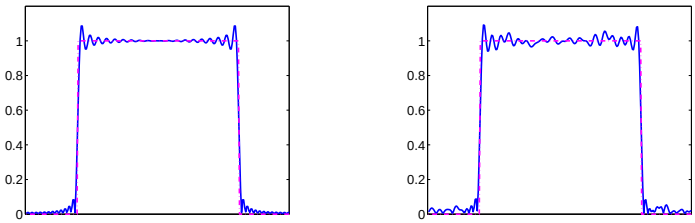

(a) ZP

(b) Noise ZP

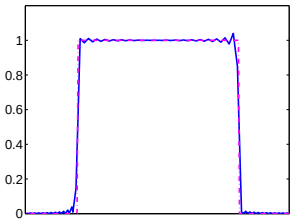

(c) BZP

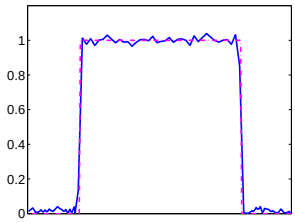

(d) Noise BZP

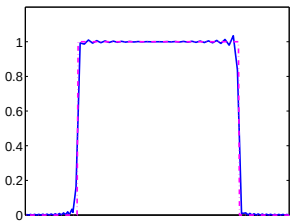

(e) BZP_Tik

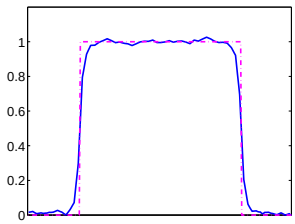

(f) Noise BZP_Tik

Figure 3.3: Test problem TP1, B-splines of degree 1 ($N_{\text{low}} = 64$).

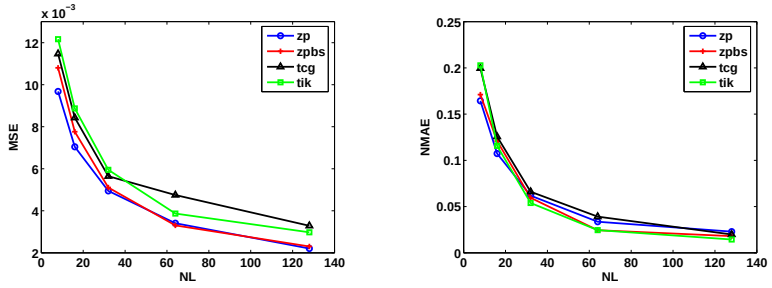

(a) MSE, no noise

(b) NMAE, no noise

Figure 3.4: Error parameters with NL varying for test problem TP1.

	No Noise		Noise	
Method	MSE	NMAE	MSE	NMAE
ZP	3.407e-3	3.362e-2	3.580e-3	4.768e-2
BZP (deg. 3)	3.306e-3	2.447e-2	3.452e-3	4.037e-2
BZP_CG (deg. 3)	4.750e-3	3.917e-2	4.795e-3	4.754e-2
BZP_Tik (deg. 3)	3.870e-3	2.450e-2	6.162e-3	6.627e-2
BZP (deg. 1)	3.463e-3	2.222e-2	3.564e-3	3.642e-2
BZP_Tik (deg. 1)	3.641e-3	2.383e-2	4.869e-3	5.076e-2

Table 3.1: Error parameters for test problem TP1.

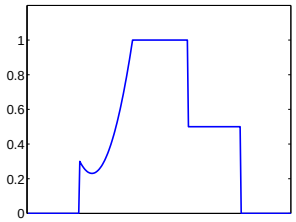

(a) Exact signal

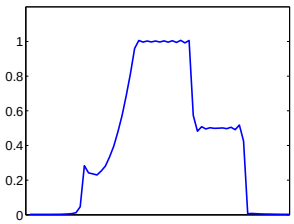

(b) Low resolution signal

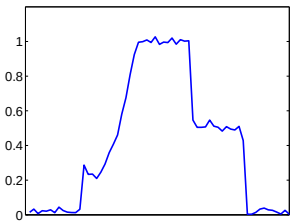

(c) Low resolution low noise signal

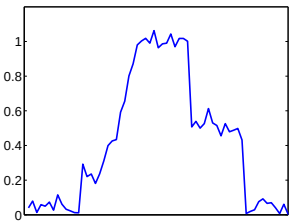

(d) Low resolution medium noise signal

Figure 3.5: Test problem TP2 ($N_{\text{low}} = 64$).

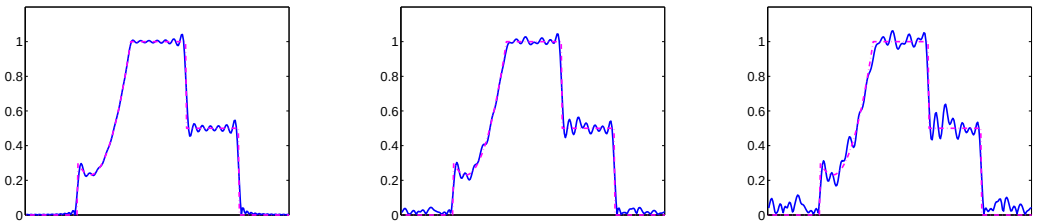

(a) ZP (b) Low Noise ZP (c) Medium Noise ZP

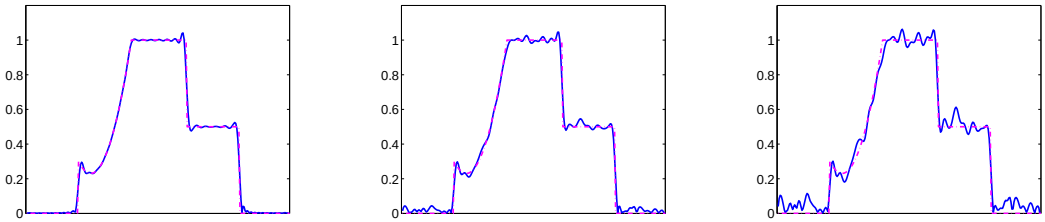

(d) BZP (e) Low Noise BZP (f) Medium Noise BZP

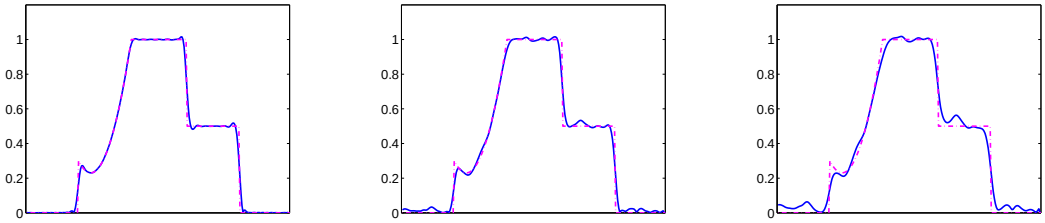

(g) BZP_Tik (h) Low Noise BZP_Tik (i) Medium Noise BZP_Tik

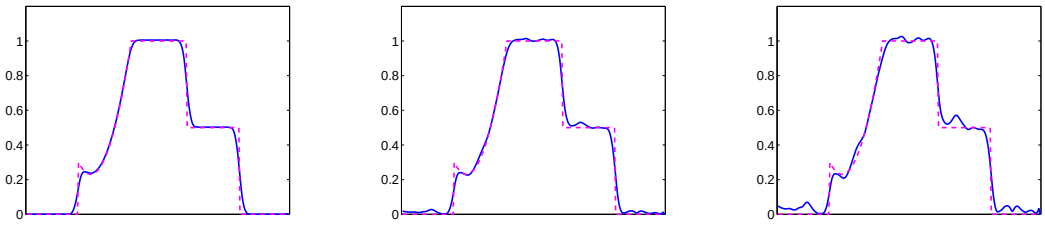

(j) BZP_CG (k) Low Noise BZP_CG (l) Medium Noise BZP_CG

Figure 3.6: Test problem TP2, B-splines of degree 3 ($N_{\text{low}} = 64$).

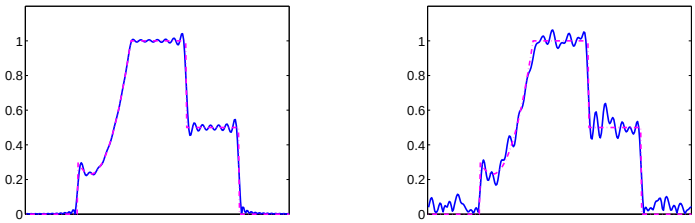

(a) ZP

(b) Medium Noise ZP

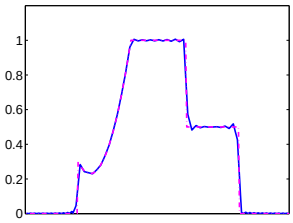

(c) BZP

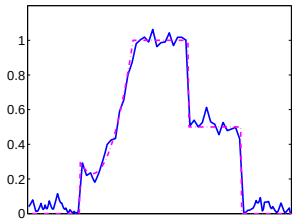

(d) Medium Noise BZP

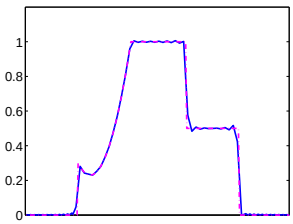

(e) BZP_Tik

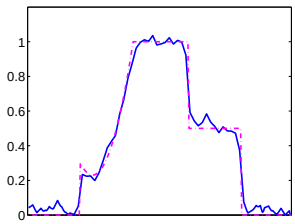

(f) Medium Noise BZP_Tik

Figure 3.7: Test problem TP2, B-splines of degree 1 ($N_{\text{low}} = 64$).

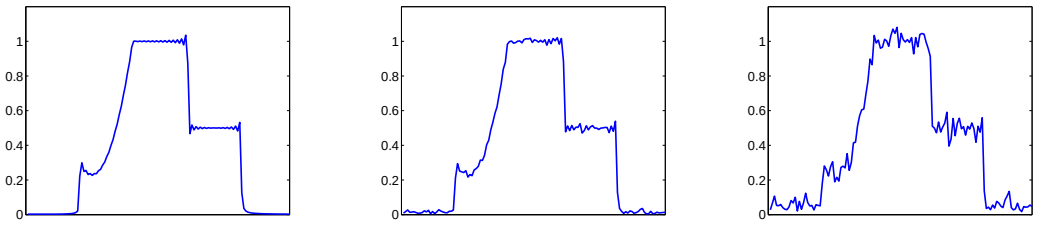

(a) Low resolution signal

(b) Low resolution low noise signal

(c) Low resolution high noise signal

Figure 3.8: Test problem TP2 ($N_{\text{low}} = 128$).

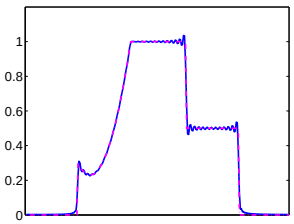

(a) ZP

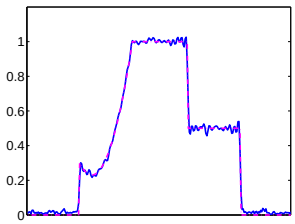

(b) Low Noise ZP

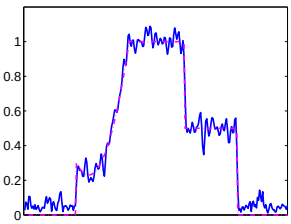

(c) High Noise ZP

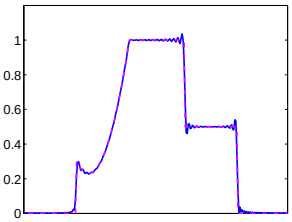

(d) BZP

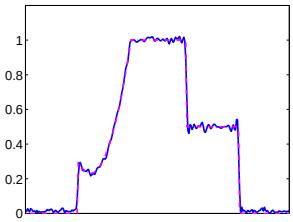

(e) Low Noise BZP

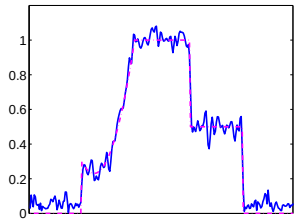

(f) High Noise BZP

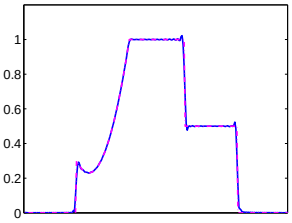

(g) BZP_Tik

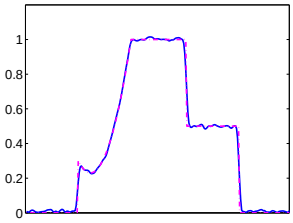

(h) Low Noise BZP_Tik

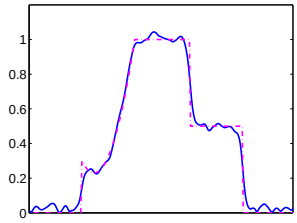

(i) High Noise BZP_Tik

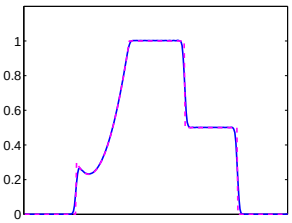

(j) BZP_CG

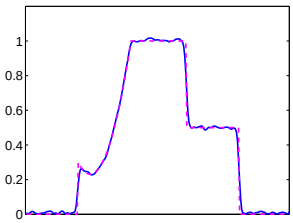

(k) Low Noise BZP_CG

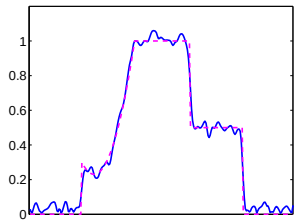

(l) High Noise BZP_CG

Figure 3.9: Test problem TP2, B-splines of degree 3 ($N_{\text{low}} = 128$).

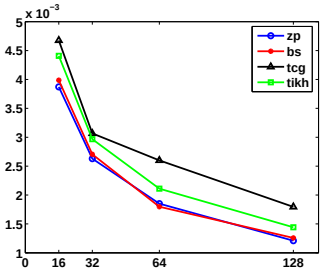

(a) MSE, degree 3, no noise

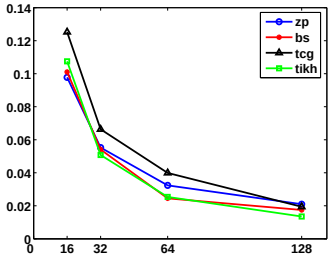

(b) NMAE, degree 3, no noise

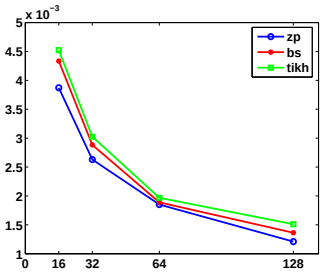

(c) MSE, degree 1, no noise

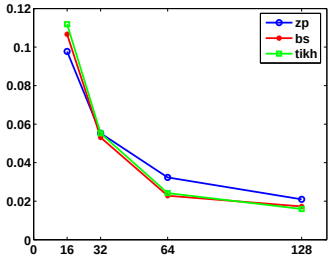

(d) NMAE, degree 1, no noise

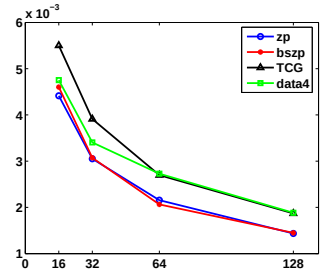

(e) MSE, degree 3, low noise

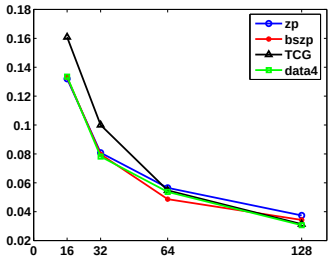

(f) NMAE, degree 3,low noise

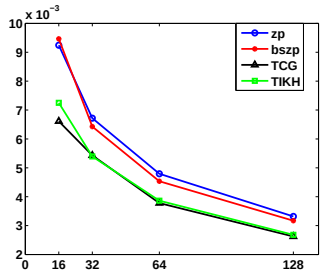

(g) MSE, degree 3, high noise

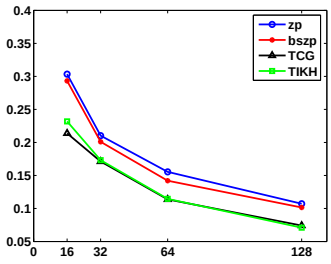

(h) NMAE, degree 3,high noise

Figure 3.10: Error parameters with N_{low} varying for test problem TP2.

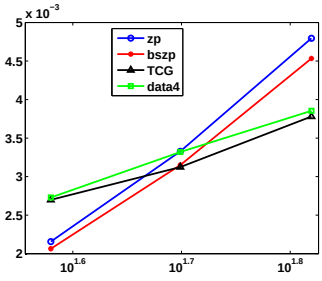

(a) MSE, degree 3, $N_{\text{low}} = 64$

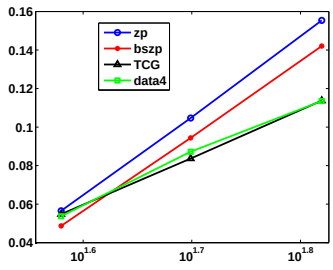

(b) NMAE, degree 3, $N_{\text{low}} = 64$

Figure 3.11: Error parameters with noise varying ($N_{\text{low}} = 64$) for test problem TP2.

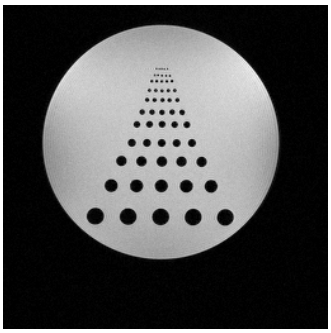

Figure 3.12: Test problem: *phantom*.

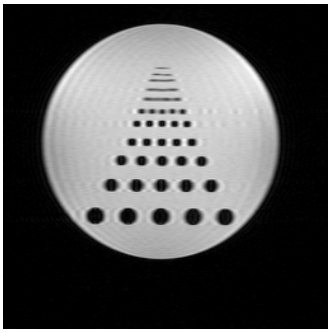

(a) ZP

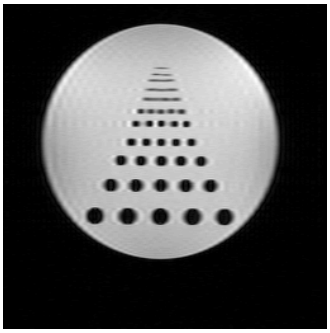

(b) BZP

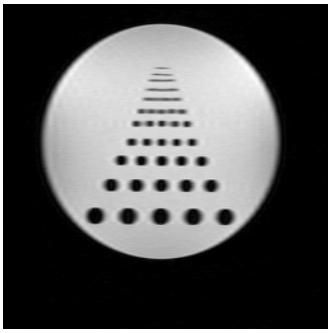

(c) BZP_Tik

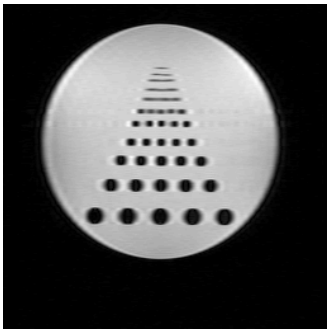

(d) BZP_CG

Figure 3.13: Test problem *phantom* (reconstructions with $N_{\text{low}} = 64$).

(a) ZP

(b) BZP

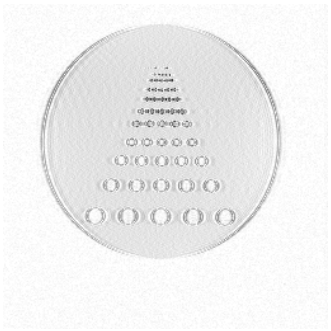

(c) BZP_Tik

(d) BZP_CG

Figure 3.14: Test problem *phantom* (difference images with $N_{\text{low}} = 64$).

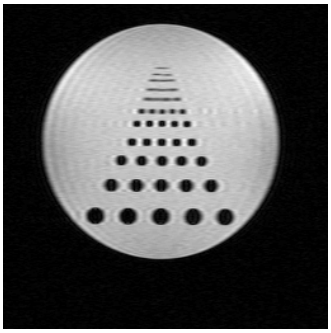

(a) ZP

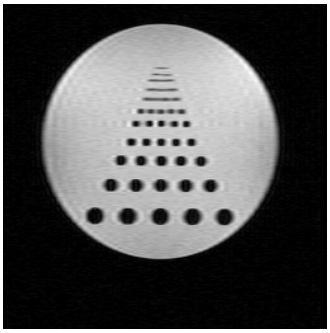

(b) BZP

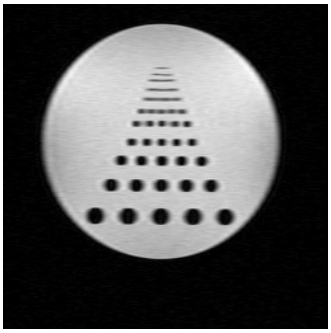

(c) BZP_Tik

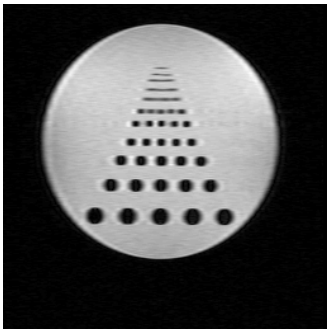

(d) BZP_CG

Figure 3.15: Test problem *phantom*, low noise (snr = 65 db) (reconstructions with $N_{\text{low}} = 64$).

(a) ZP

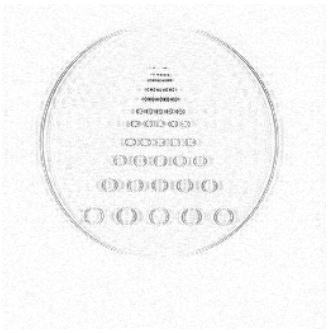

(b) BZP

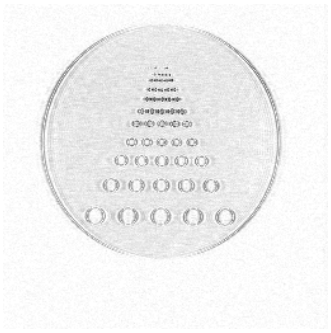

(c) BZP_Tik

(d) BZP_CG

Figure 3.16: Test problem *phantom*, low noise (snr = 65 db) (difference images with $N_{\text{low}} = 64$).

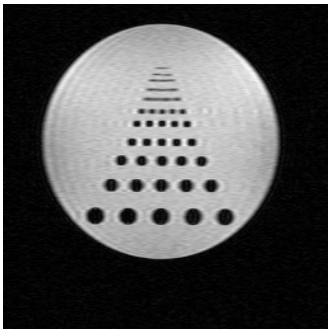

(a) ZP

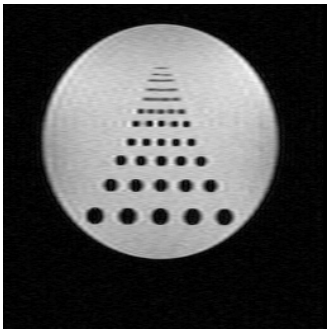

(b) BZP

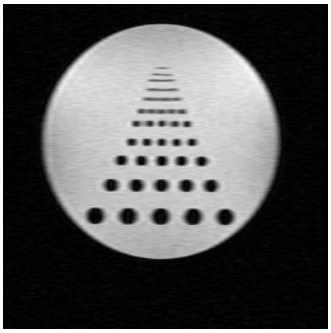

(c) BZP_Tik

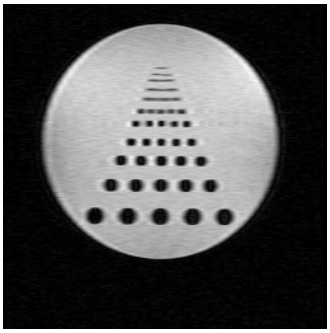

(d) BZP_CG

Figure 3.17: Test problem *phantom*, medium noise (snr = 58 db) (reconstructions with $N_{\text{low}} = 64$).

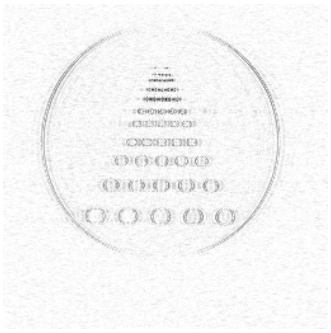

(a) ZP

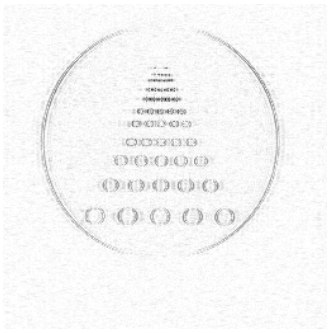

(b) BZP

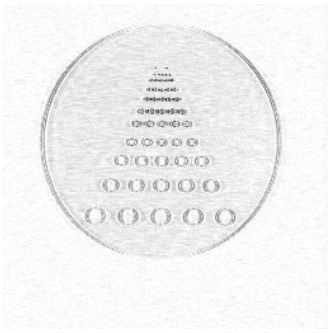

(c) BZP_Tik

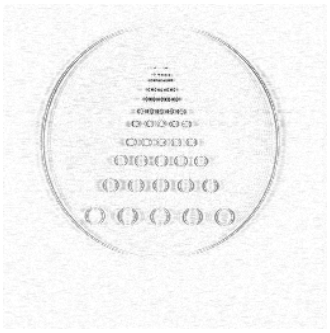

(d) BZP_CG

Figure 3.18: Test problem *phantom*, medium noise (snr = 58 db) (difference images with $N_{\text{low}} = 64$).

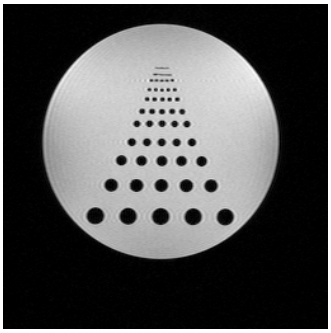

(a) ZP

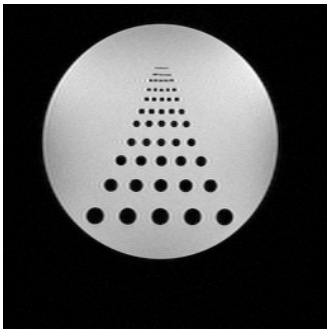

(b) BZP

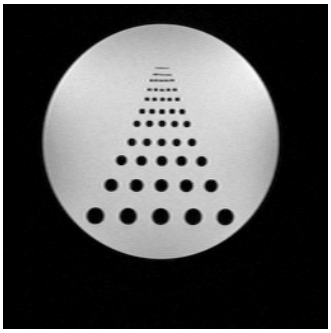

(c) BZP_Tik

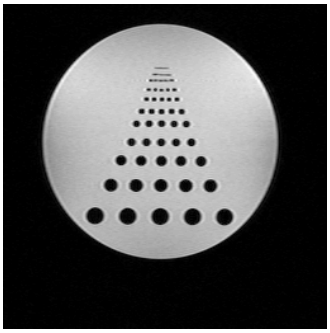

(d) BZP_CG

Figure 3.19: Test problem *phantom* (reconstructions with $N_{\text{low}} = 128$).

(a) ZP

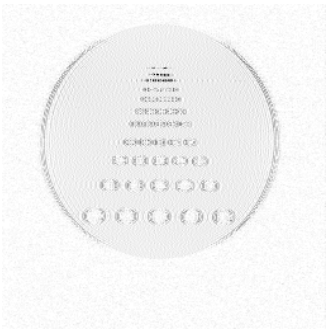

(b) BZP

(c) BZP_Tik

(d) BZP_CG

Figure 3.20: Test problem *phantom* (difference images with $N_{\text{low}} = 128$).

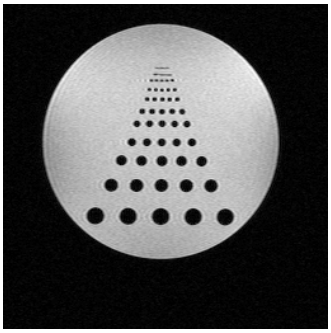

(a) ZP

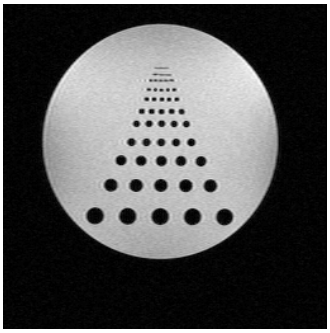

(b) BZP

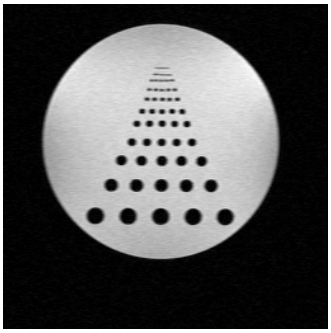

(c) BZP_Tik

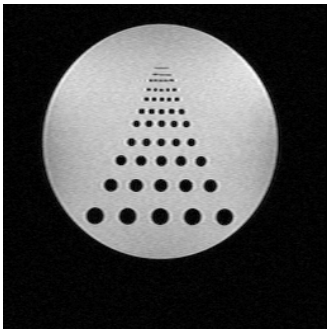

(d) BZP_CG

Figure 3.21: Test problem *phantom*, medium noise (snr = 58 db) (reconstructions with $N_{\text{low}} = 128$).

(a) ZP

(b) BZP

(c) BZP_Tik

(d) BZP_CG

Figure 3.22: Test problem *phantom*, medium noise (snr = 58 db) (difference images with $N_{\text{low}} = 128$).

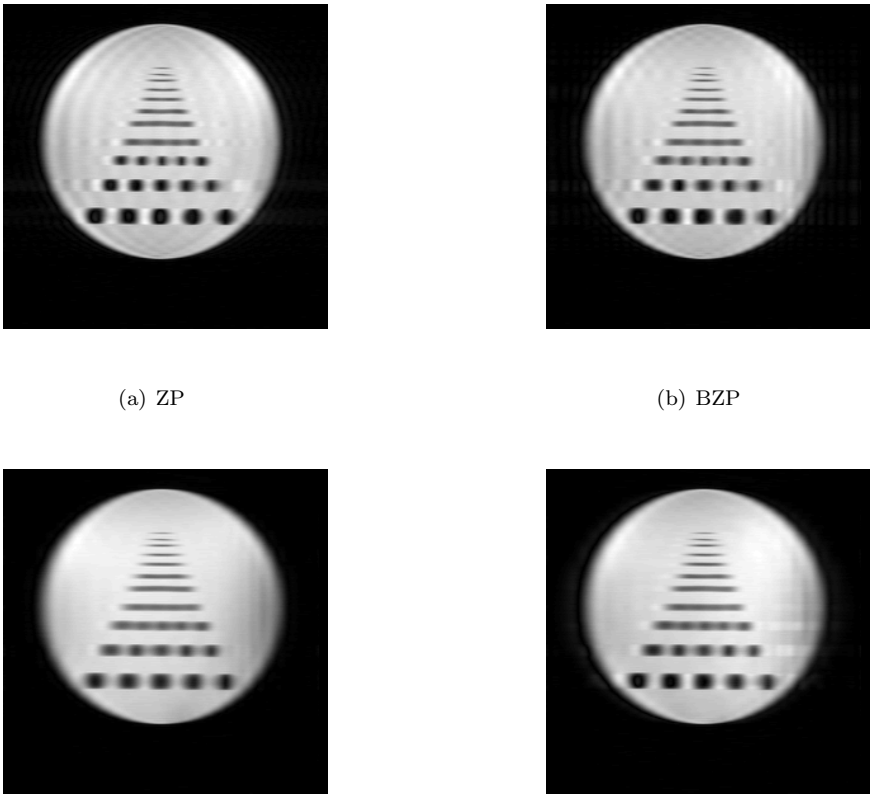

(a) ZP

(b) BZP

(c) BZP_Tik

(d) BZP_CG

Figure 3.23: Test problem *phantom*, medium noise (snr = 58 db) (reconstructions with $N_{\text{low}} = 32$).

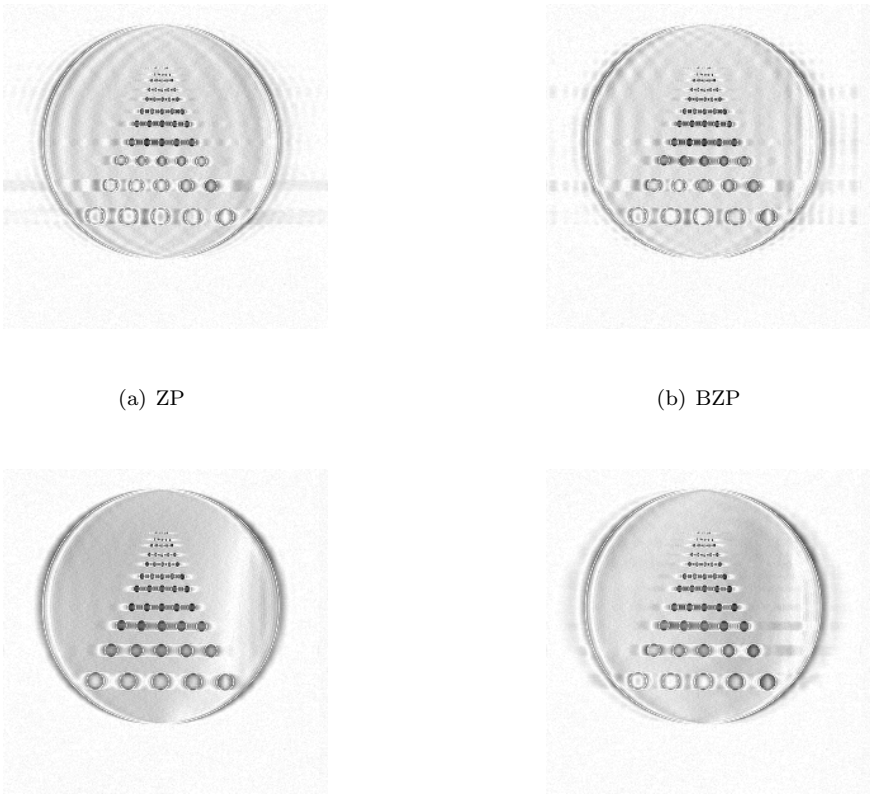

(a) ZP

(b) BZP

(c) BZP_Tik

(d) BZP_CG

Figure 3.24: Test problem *phantom*, medium noise (snr = 58 db) (difference images with $N_{\text{low}} = 32$).

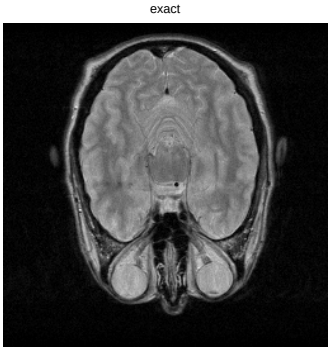

Figure 3.25: Test problem: *brain*.

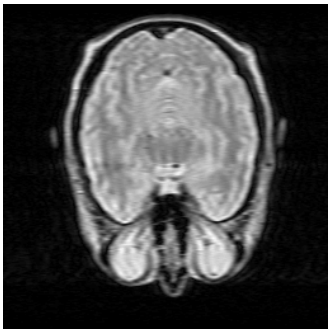

(a) ZP

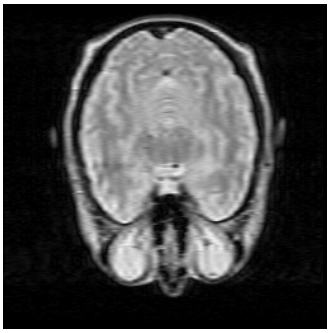

(b) BZP

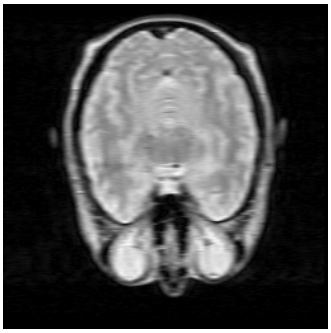

(c) BZP_Tik

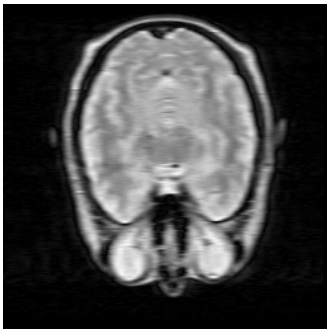

(d) BZP_CG

Figure 3.26: Test problem *brain* (reconstructions with $N_{\text{low}} = 64$).

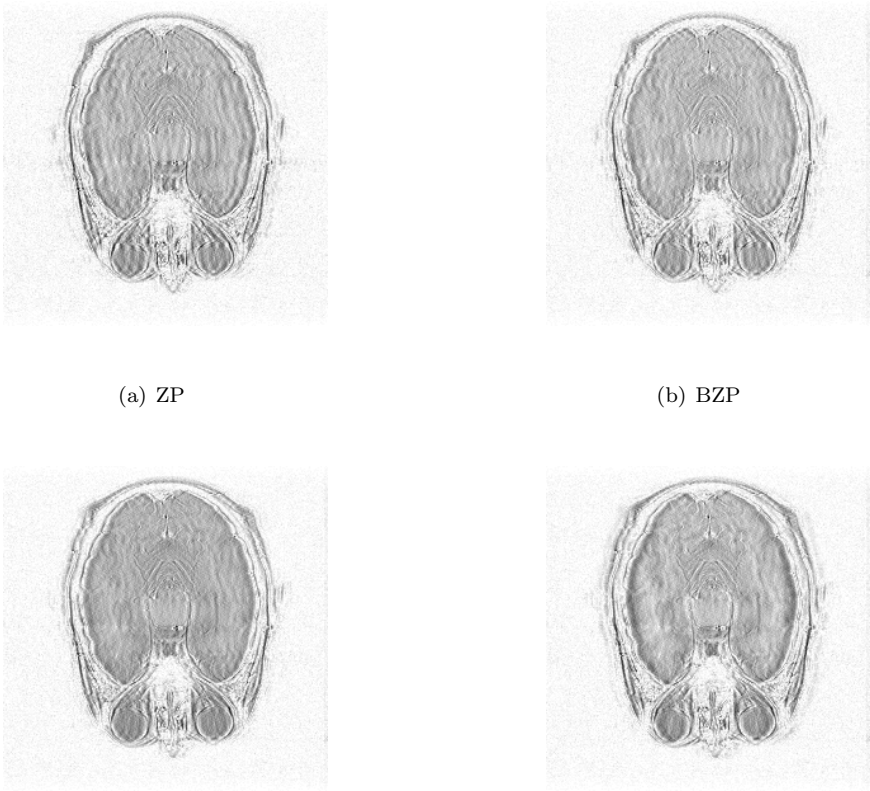

(a) ZP (b) BZP

(c) BZP_Tik (d) BZP_CG

Figure 3.27: Test problem *brain* (difference images with $N_{\text{low}} = 64$).

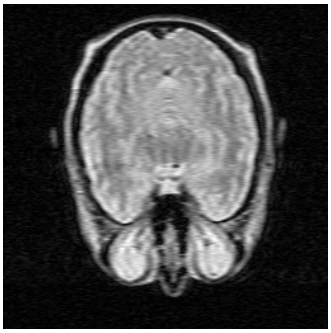

(a) ZP

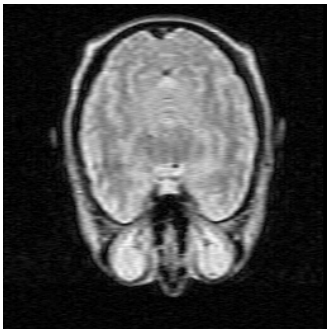

(b) BZP

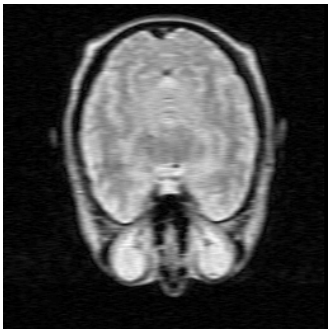

(c) BZP_Tik

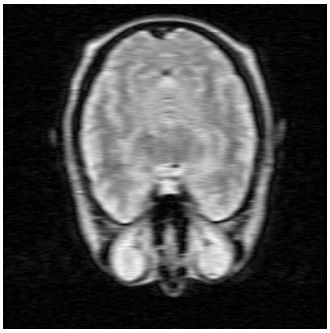

(d) BZP_CG

Figure 3.28: Test problem *brain* with noise (snr=49 db) (reconstructions with $N_{\text{low}} = 64$).

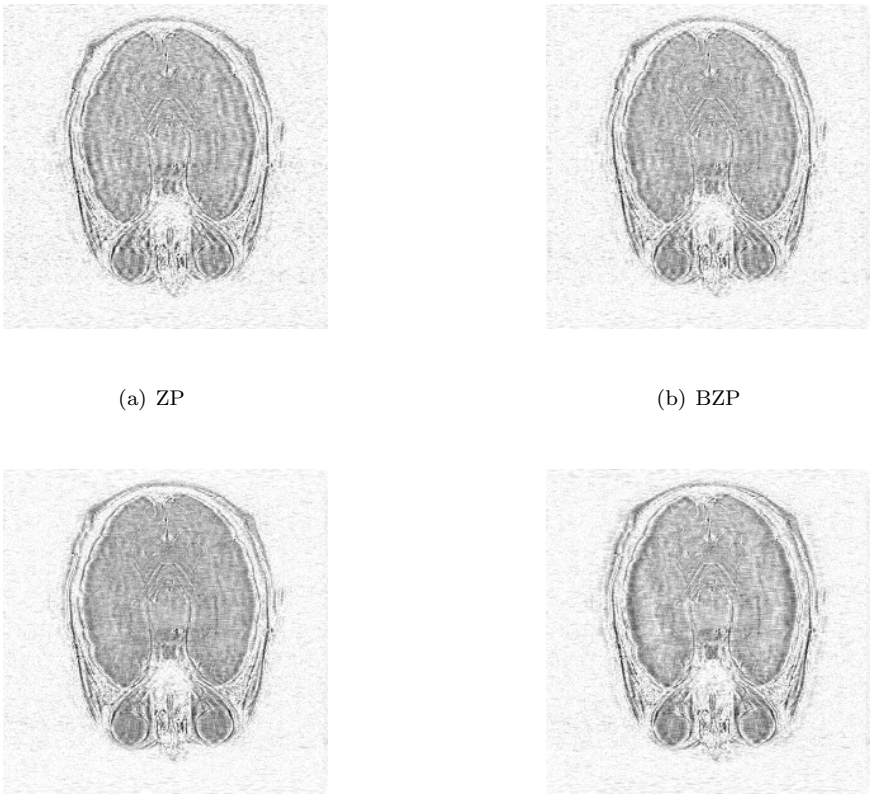

(a) ZP

(b) BZP

(c) BZP_Tik

(d) BZP_CG

Figure 3.29: Test problem *brain* with noise (snr=49 db) (difference images with $N_{\text{low}} = 64$).

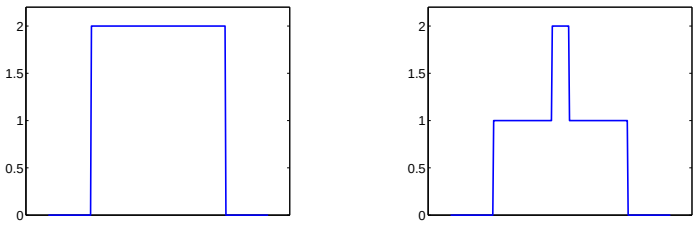

(a) Reference signal (b) Dynamic signal

Figure 3.30: Test problem TP3

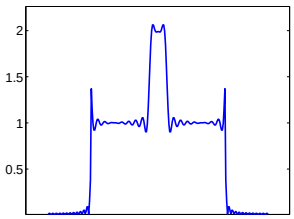

(a) KEY, $N_{\text{low}} = 64$

(b) BKEY, $N_{\text{low}} = 64$

(c) BKEY_Tik, $N_{\text{low}} = 64$

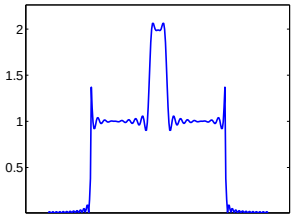

(d) KEY, $N_{\text{low}} = 64$

(e) BKEY, $N_{\text{low}} = 64$, deg=1

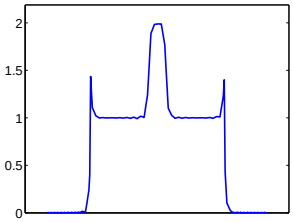

(f) BKEY_Tik, $N_{\text{low}} = 64$, deg=1

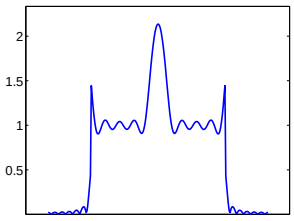

(g) KEY, $N_{\text{low}} = 32$

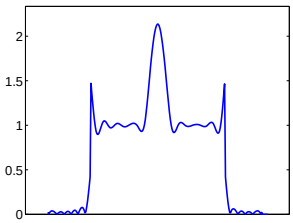

(h) BKEY, $N_{\text{low}} = 32$

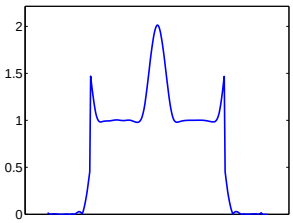

(i) BKEY_Tik, $N_{\text{low}} = 32$

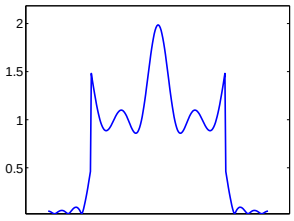

(j) KEY, $N_{\text{low}} = 16$

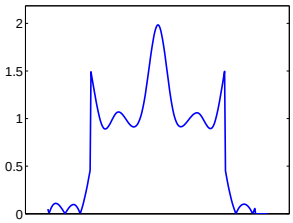

(k) BKEY, $N_{\text{low}} = 16$

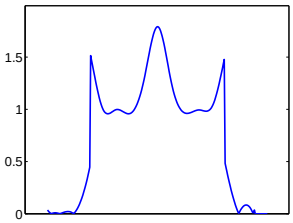

(l) BKEY_Tik, $N_{\text{low}} = 16$

Figure 3.31: Test problem TP3, Keyhole-like methods, reconstructions with N_{low} varying.

(a) BRIGR,$N_{\text{low}} = 64$

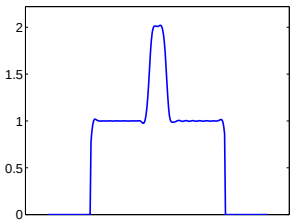

(b) BRIGR_Tik, $N_{\text{low}} = 64$

(c) RIGR, $N_{\text{low}} = 64$

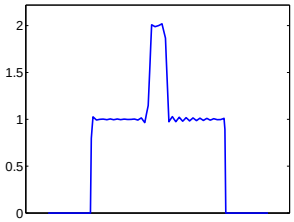

(d) BRIGR, $N_{\text{low}} = 64$, deg=1

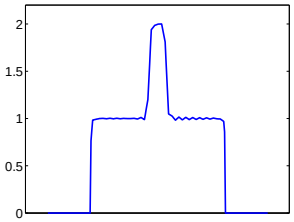

(e) BRIGR_Tik, $N_{\text{low}} = 64$, deg=1

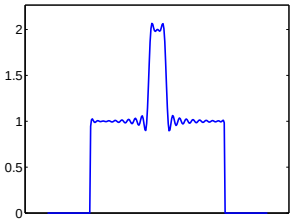

(f) RIGR, $N_{\text{low}} = 64$

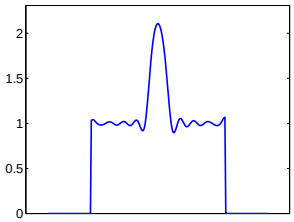

(g) BRIGR, $N_{\text{low}} = 32$

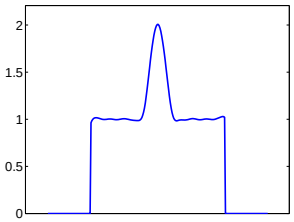

(h) BRIGR_Tik, $N_{\text{low}} = 32$

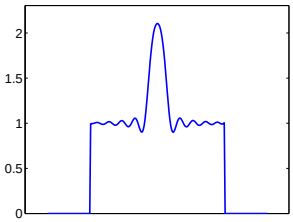

(i) RIGR, $N_{\text{low}} = 32$

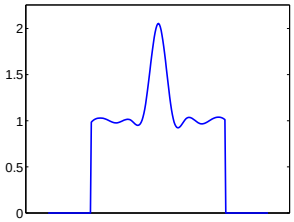

(j) BRIGR,$N_{\text{low}} = 16$

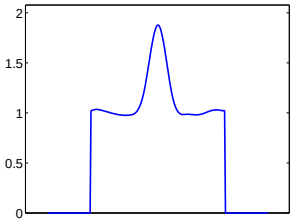

(k) BRIGR_Tik, $N_{\text{low}} = 16$

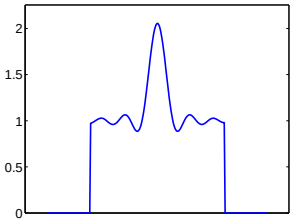

(l) RIGR, $N_{\text{low}} = 16$

Figure 3.32: Test problem TP3, RIGR-like methods, reconstructions with N_{low} varying.

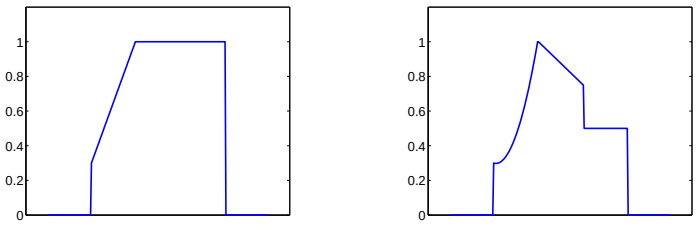

(a) Reference signal (b) Dynamic signal

Figure 3.33: Test problem TP4

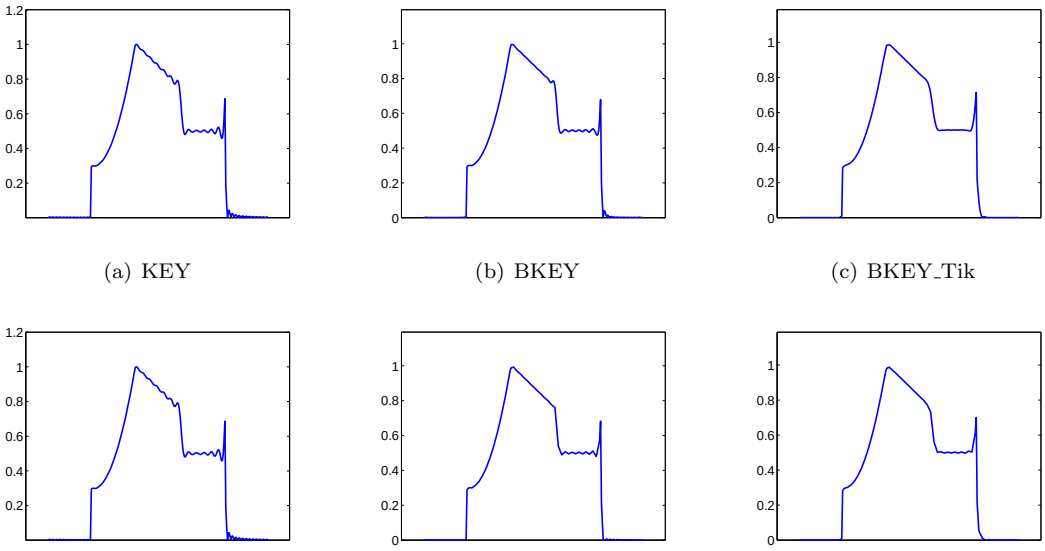

(a) KEY (b) BKEY (c) BKEY_Tik

(d) KEY (e) BKEY, deg=1 (f) BKEY_Tik, deg=1

Figure 3.34: Test problem TP4, Keyhole-like methods, reconstructions with N_{low} varying.

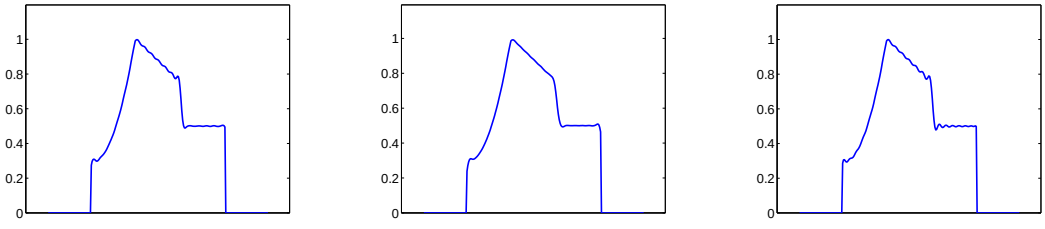

(a) BRIGR (b) BRIGR_Tik (c) RIGR

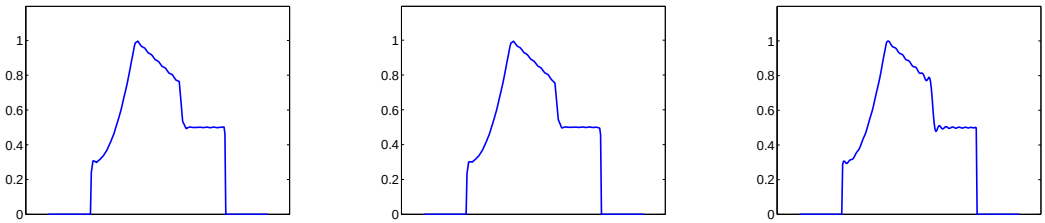

(d) BRIGR, deg=1 (e) BRIGR_Tik, deg=1 (f) RIGR

Figure 3.35: Test problem TP4, RIGR-like methods, reconstructions with N_{low} varying.

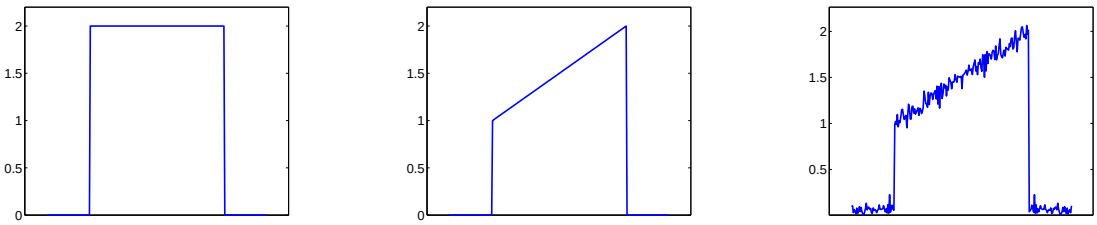

(a) Reference signal (b) Dynamic signal (c) Dynamic signal with noise

Figure 3.36: Test problem TP5.

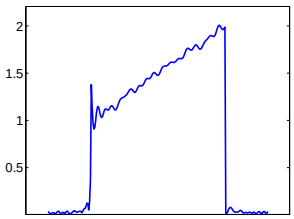

(a) KEY, $N_{\text{low}} = 64$

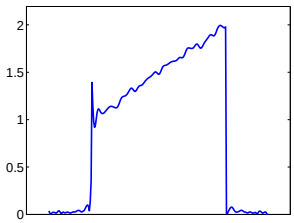

(b) BKEY, $N_{\text{low}} = 64$

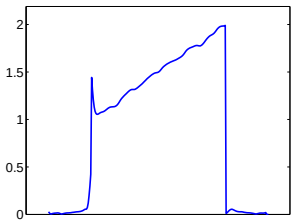

(c) BKEY_Tik, $N_{\text{low}} = 64$

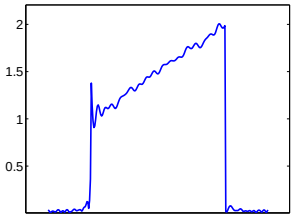

(d) KEY, $N_{\text{low}} = 64$, deg=1

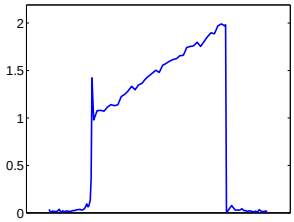

(e) BKEY, $N_{\text{low}} = 64$, deg=1

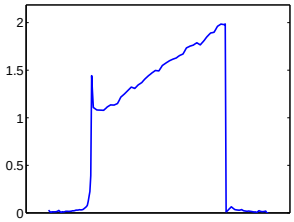

(f) BKEY_Tik, $N_{\text{low}} = 64$, deg=1

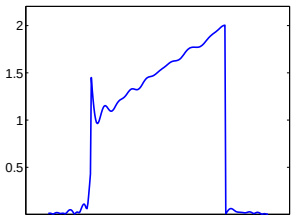

(g) KEY, $N_{\text{low}} = 32$

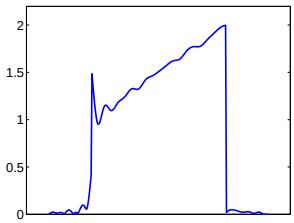

(h) BKEY, $N_{\text{low}} = 32$

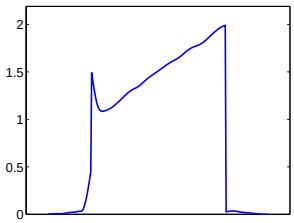

(i) BKEY_Tik, $N_{\text{low}} = 32$

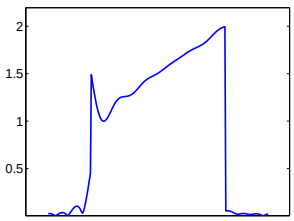

(j) KEY, $N_{\text{low}} = 16$

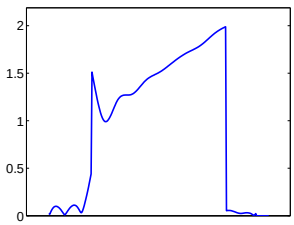

(k) BKEY, $N_{\text{low}} = 16$

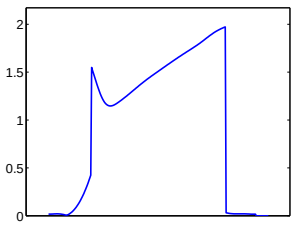

(l) BKEY_Tik, $N_{\text{low}} = 16$

Figure 3.37: Test problem TP5, Keyhole-like methods, reconstructions with N_{low} varying.

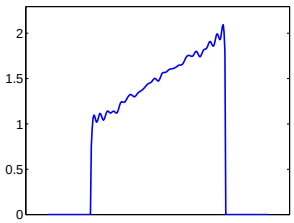

(a) BRIGR, $N_{\text{low}} = 64$

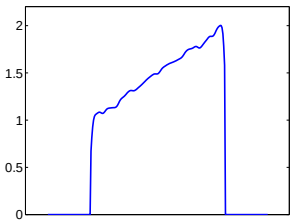

(b) BRIGR_Tik, $N_{\text{low}} = 64$

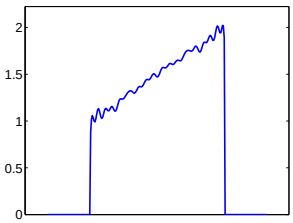

(c) RIGR, $N_{\text{low}} = 64$

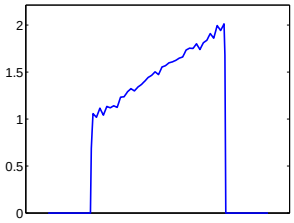

(d) BRIGR, $N_{\text{low}} = 64$, deg=1

(e) BRIGR_Tik, $N_{\text{low}} = 64$, deg=1

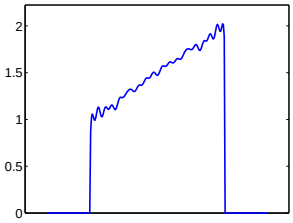

(f) RIGR, $N_{\text{low}} = 64$, deg=1

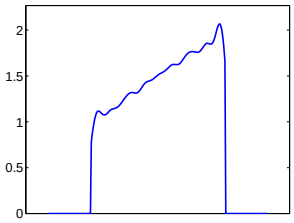

(g) BRIGR, $N_{\text{low}} = 32$

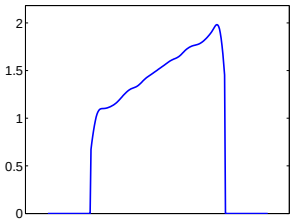

(h) BRIGR_Tik, $N_{\text{low}} = 32$

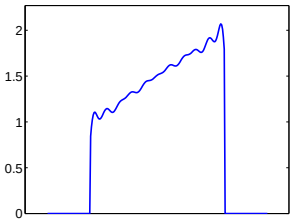

(i) RIGR, $N_{\text{low}} = 32$

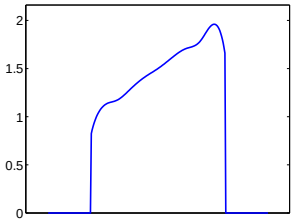

(j) BRIGR, $N_{\text{low}} = 16$

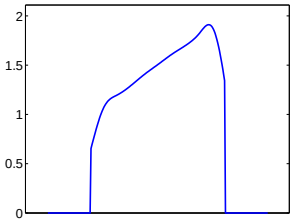

(k) BRIGR_Tik, $N_{\text{low}} = 16$

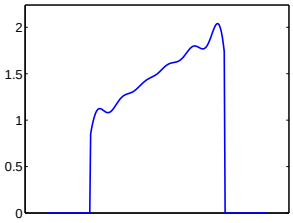

(l) RIGR, $N_{\text{low}} = 16$

Figure 3.38: Test problem TP5, RIGR-like methods, reconstructions with N_{low} varying.

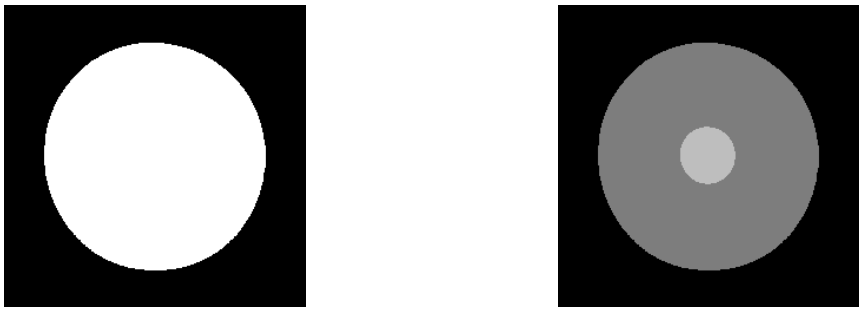

(a) Reference image (b) Dynamic image

Figure 3.39: Test problem: *circle*.

(a) KEY, $N_{\text{low}} = 64$

(b) BKEY, $N_{\text{low}} = 64$

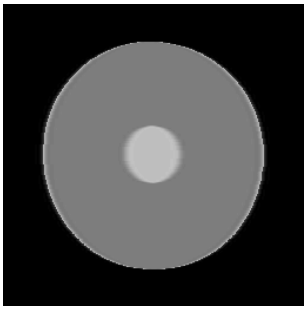

(c) BKEY_Tik, $N_{\text{low}} = 64$

Figure 3.40: Test problem *circle*, Keyhole-like methods (reconstructions with $N_{\text{low}} = 64$).

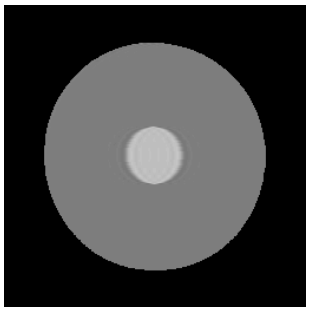

(a) RIGR, $N_{\text{low}} = 64$

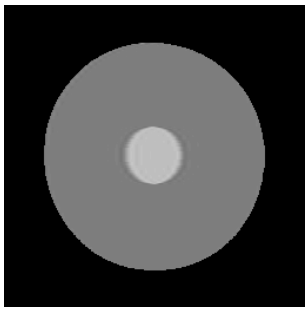

(b) BRIGR,$N_{\text{low}} = 64$

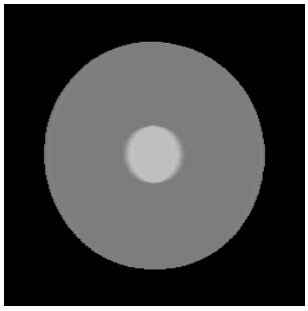

(c) BRIGR_Tik, $N_{\text{low}} = 64$

Figure 3.41: Test problem *circle*, RIGR-like methods (reconstructions with $N_{\text{low}} = 64$).

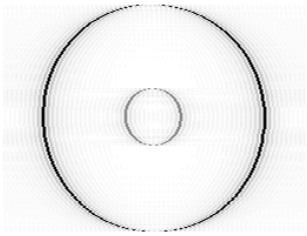

(a) KEY, $N_{\text{low}} = 64$

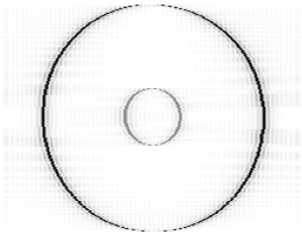

(b) BKEY, $N_{\text{low}} = 64$

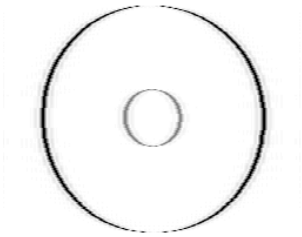

(c) BKEY_Tik, $N_{\text{low}} = 64$

Figure 3.42: Test problem *circle*, Keyhole-like methods (difference images with $N_{\text{low}} = 64$).

(a) RIGR, $N_{\text{low}} = 64$

(b) BRIGR, $N_{\text{low}} = 64$

(c) BRIGR_Tik, $N_{\text{low}} = 64$

Figure 3.43: Test problem *circle*, RIGR-like methods (difference images with $N_{\text{low}} = 64$).

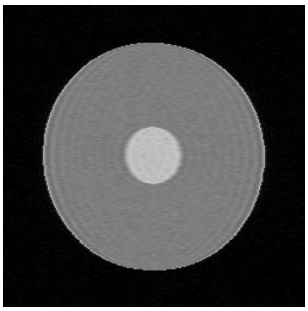

(a) KEY, $N_{\text{low}} = 64$

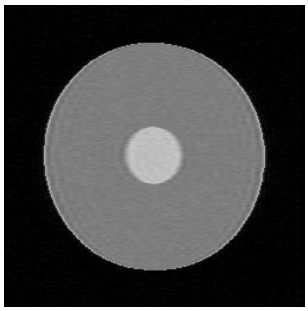

(b) BKEY, $N_{\text{low}} = 64$

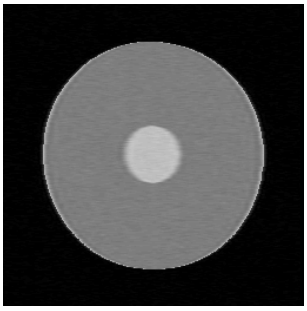

(c) BKREY_Tik, $N_{\text{low}} = 64$

Figure 3.44: Test problem *circle* with noise, Keyhole-like methods (reconstructions with $N_{\text{low}} = 64$).

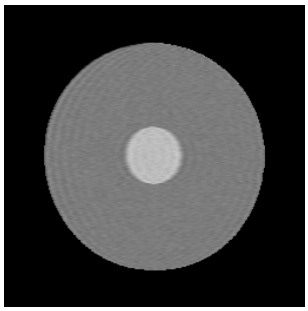

(a) RIGR, $N_{\text{low}} = 64$

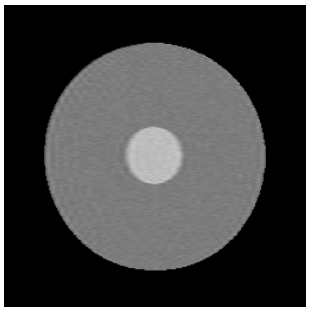

(b) BRIGR, $N_{\text{low}} = 64$

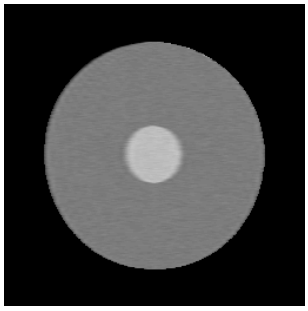

(c) BRIGR_Tik, $N_{\text{low}} = 64$

Figure 3.45: Test problem *circle* with noise, RIGR-like methods (reconstructions with $N_{\text{low}} = 64$).

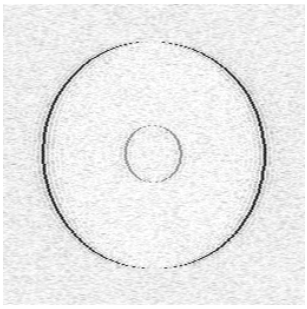

(a) KEY, $N_{\text{low}} = 64$

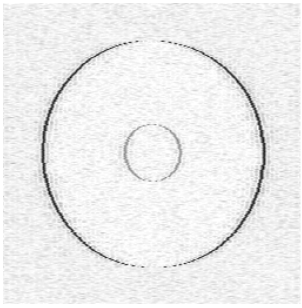

(b) BKEY, $N_{\text{low}} = 64$

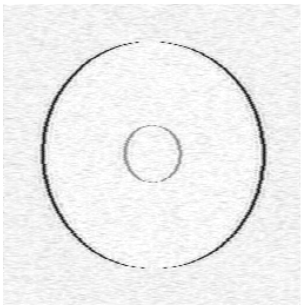

(c) BKEY_Tik, $Nl = 64$

Figure 3.46: Test problem *circle* with noise, Keyhole-like methods (difference images with $N_{\text{low}} = 64$).

(a) RIGR, $N_{\text{low}} = 64$

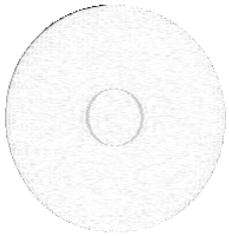

(b) BRIGR, $N_{\text{low}} = 64$

(c) BRIGR_Tik, $N_{\text{low}} = 64$

Figure 3.47: Test problem *circle* with noise, RIGR-like methods (difference images with $N_{\text{low}} = 64$).

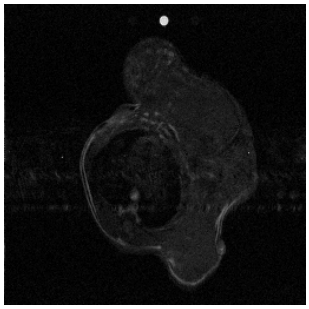

(a) Baseline reference image $I_B(\boldsymbol{x}, \boldsymbol{y})$

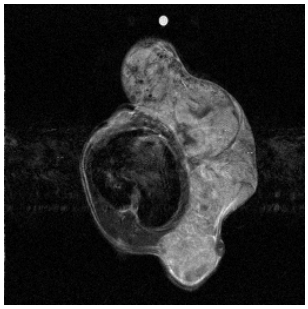

(b) Active reference image $I_A(\boldsymbol{x}, \boldsymbol{y})$

Figure 3.48: Test problem: *mouse* (real data)

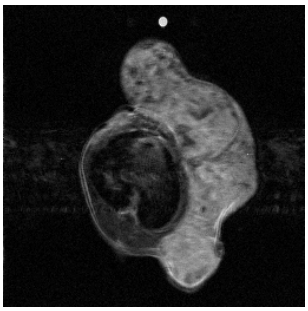

(a) KEY, $N_{\text{low}} = 64$

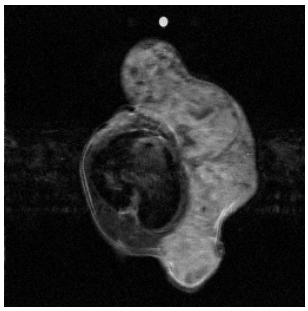

(b) BKEY, $N_{\text{low}} = 64$

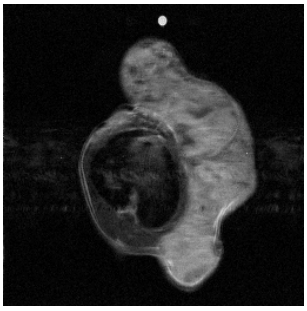

(c) BKEY_Tik, $N_{\text{low}} = 64$

Figure 3.49: Test problem *mouse*, Keyhole-like methods (reconstructions with $N_{\text{low}} = 64$).

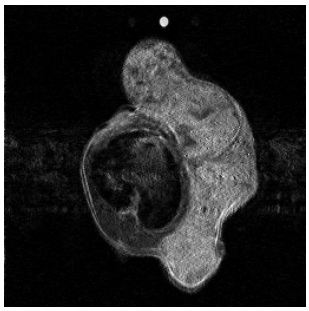

(a) RIGR, $N_{\text{low}} = 64$

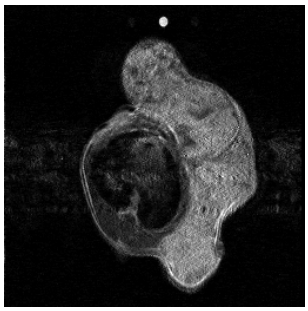

(b) BRIGR,$N_{\text{low}} = 64$

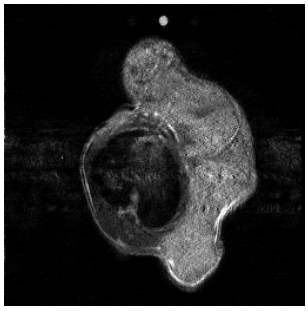

(c) BRIGR_Tik, $N_{\text{low}} = 64$

Figure 3.50: Test problem *mouse*, RIGR-like methods (reconstructions with $N_{\text{low}} = 64$).

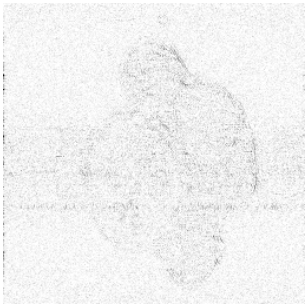

(a) KEY, $N_{\text{low}} = 64$

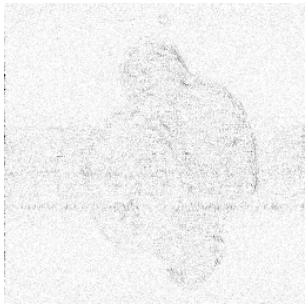

(b) BKEY, $N_{\text{low}} = 64$

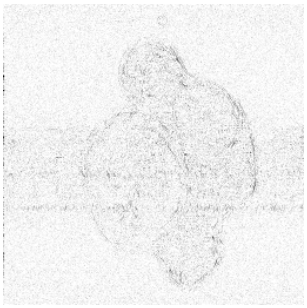

(c) BKEY_Tik, $N_{\text{low}} = 64$

Figure 3.51: Test problem *mouse*, Keyhole-like methods (difference images with $N_{\text{low}} = 64$).

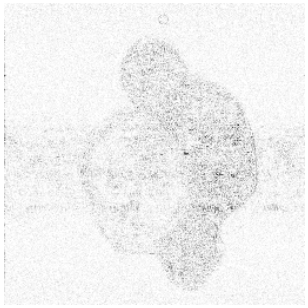

(a) RIGR, $N_{\text{low}} = 64$

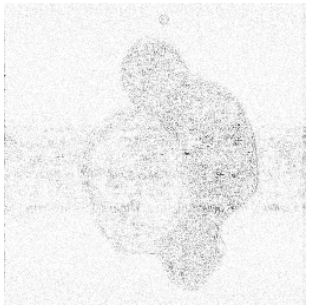

(b) BRIGR,$N_{\text{low}} = 64$

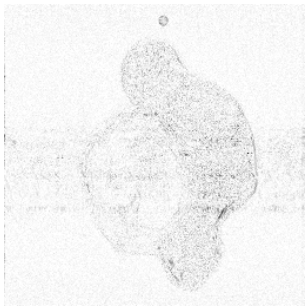

(c) BRIGR_Tik, $N_{\text{low}} = 64$

Figure 3.52: Test problem *mouse*, RIGR-like methods (difference images with $N_{\text{low}} = 64$).

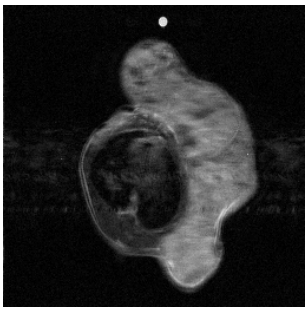

(a) KEY, $N_{\text{low}} = 32$

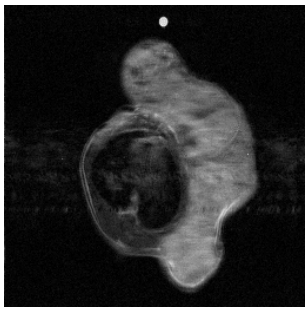

(b) BKEY, $N_{\text{low}} = 32$

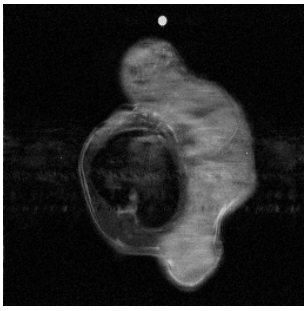

(c) BKEY_Tik, $N_{\text{low}} = 32$

Figure 3.53: Test problem *mouse*, Keyhole-like methods (reconstructions with $N_{\text{low}} = 32$).

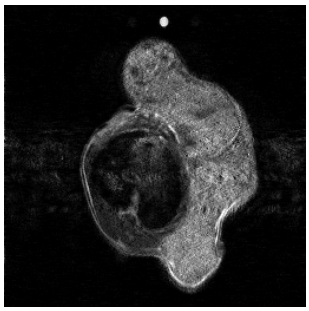

(a) RIGR, $N_{\text{low}} = 32$

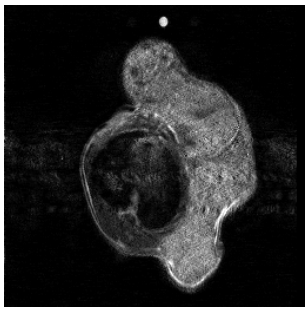

(b) BRIGR,$N_{\text{low}} = 32$

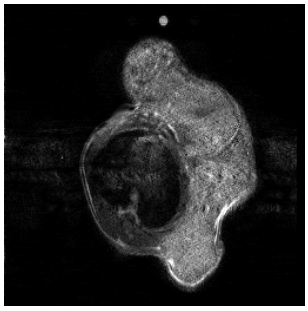

(c) BRIGR_Tik, $N_{\text{low}} = 32$

Figure 3.54: Test problem *mouse*, RIGR-like methods (reconstructions with $N_{\text{low}} = 32$).

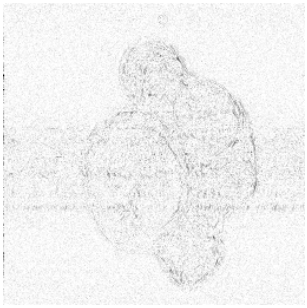

(a) KEY, $N_{\text{low}} = 32$

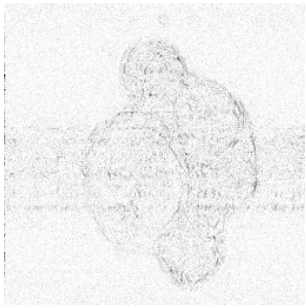

(b) BKEY, $N_{\text{low}} = 32$

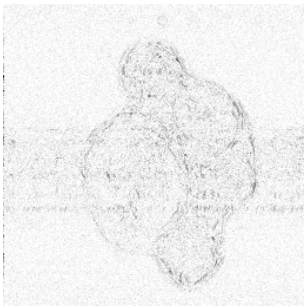

(c) BKEY_Tik, $N_{\text{low}} = 32$

Figure 3.55: Test problem *mouse*, Keyhole-like methods (difference images with $N_{\text{low}} = 32$).

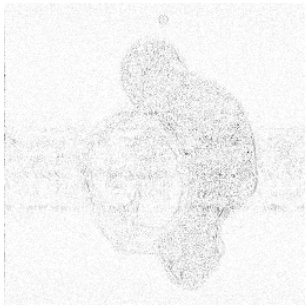

(a) RIGR, $N_{\text{low}} = 32$

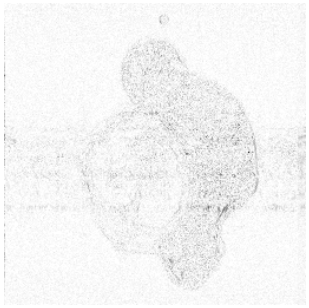

(b) BRIGR,$N_{\text{low}} = 32$

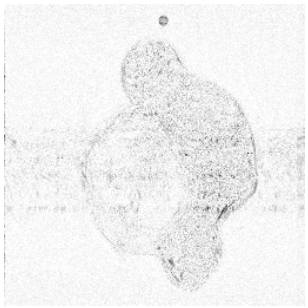

(c) BRIGR_Tik, $N_{\text{low}} = 32$

Figure 3.56: Test problem *mouse*, RIGR-like methods (difference images with $N_{\text{low}} = 32$).

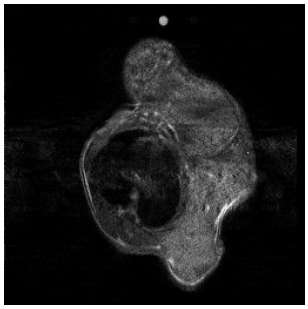

(a) section 1

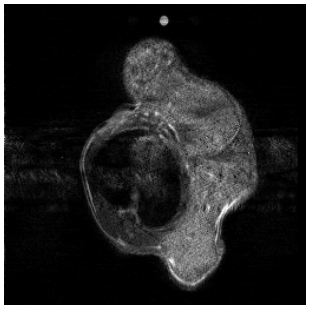

(b) section 3 $N_{\text{low}} = 32$

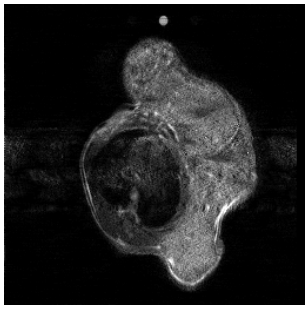

(c) section 4, $N_{\text{low}} = 32$

Figure 3.57: Test problem *mouse*, TBRIGR_Tik method (reconstructions with $N_{\text{low}} = 64$).

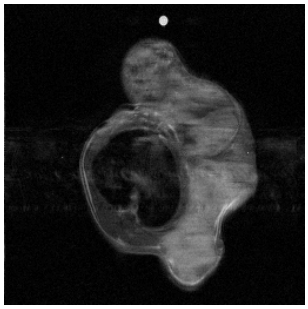

(a) section 1

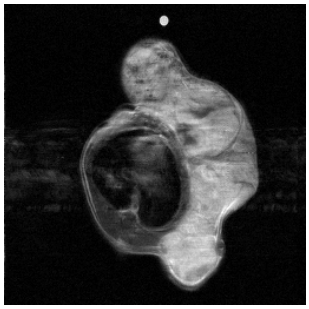

(b) section 3

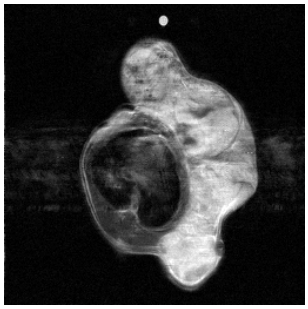

(c) section 4

Figure 3.58: Test problem *mouse*, WBKEY_Tik method (reconstructions with $N_{\text{low}} = 64$).

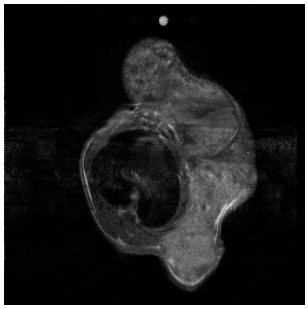

(a) section 1

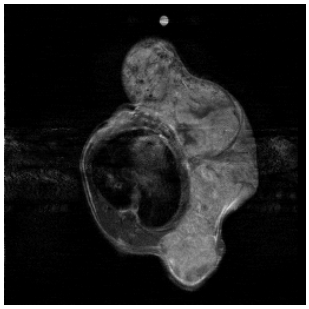

(b) section 3

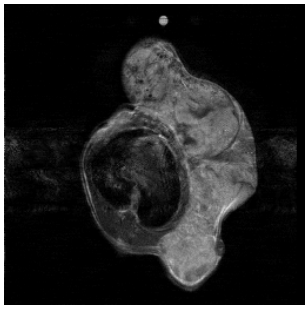

(c) section 4

Figure 3.59: Test problem *mouse*, WBRIGR_Tik method (reconstructions with $N_{\text{low}} = 64$).

Bibliography

[1] A. Björck. *Numerical Methods for Least Squares Problems*. SIAM, Philadelphia, 1996.

[2] Y.P. Du, D.L. Parker, et al. Reduction of partial-volume artifacts with zero-filled interpolation in three-dimensional mr angiography. *J. Magn. Reson. Imaging*, 4:733–741, 1994.

[3] J.M. Hanson, Z.P. Liang, et al. Fast dynamic imaging using two reference images. *Magn. Res. Med.*, 36:172–175, 1996.

[4] X. Hu. On the "Keyhole" technique. *Journal Magn. Resonance Imag.*, 4(2):231, 1994.

[5] Tsao J, B. Behnia, and A.G. Webb. Unifying linear prior-information driven methods for accelerated image acquisition. *Magn. Reson. Med.*, 46:652–660, 2001.

[6] R.A. Jones, O. Haraldseth, et al. K-space substitution: a novel dynamic imaging technique. *Magn. Reson. Med.*, 29:830–834, 1993.

[7] I. Kumar, D. Welti, and R.R. Ernst. NMR Fourier zeugmatography. *J. Magn. Reson.*, pages 18–69, 1975.

[8] Z-P. Liang and P.C. Lauterbur. An efficient method for dynamic magnetic resonance imaging. *IEEE trans. on Med. Imaging*, 13(4):677–686, 1994.

[9] Z.P. Liang and P.C. Lauterbur. An efficient method for Dynamic Magnetic Resonance Imaging. *IEEE Trans. Med. Imag.*, 13:677–686, 1994.

[10] Z.P. Liang, B. Madore, G.H. Glover, and N.J. Pelc. Fast algorithms for GS-model-based image reconstruction in data-sharing Fourier imaging. *IEEE Trans. Med. Imag.*, 22(8):1026–1030, 2003.

[11] P. Mansfield. Multi planar image formation using NMR spin echoes. *J. Phys C*, 10:55–58, 1977.

[12] E. Loli Piccolomini, G. Landi, and F. Zama. A B–spline parametric model for high resolution dynamic Magnetic Resonance Imaging. *Applied Mathematics and Computation*, 164:133–148, 2005.

[13] L. L. Schumaker. *Spline functions: basic theory*. John Wiley and Sons, Inc., New York, 1981.

[14] M. Unser. Splines: a perfect fit for signal and image processing. *IEEE Signal processing magazine*, 16:22–38, 1999.

[15] J.J. van Vaals et al. "Keyhole" method for accelerating imaging of contrast agent uptake. *J. Magn. Reson. Imaging*, 3:671675, 1993.